Atmospheric Environment 366 (2026) 121713

Contents lists available at ScienceDirect

Atmospheric Environment

journal homepage: www.elsevier.com/locate/atmosenv

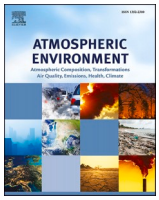

Integrating surface-based in-situ and satellite observations to characterize CO_2 and CH_4 emission hotspots in Houston, USA

Irfan Karim [a,b,*], Bernhard Rappenglück [a,b]

[a] Department of Earth and Atmospheric Sciences, University of Houston, Houston, TX, USA
[b] Institute for Climate and Atmospheric Science, University of Houston, Houston, TX, USA

HIGHLIGHTS

- Ground-based ΔCO_2 and ΔCH_4 maps reveal sharp emission hotspots that satellites often miss.
- Seasonal patterns in CO_2 and CH_4 reflect biogenic uptake and atmospheric oxidation.
- Local emissions peak in winter and fall, indicating strong seasonal variability.
- Observed $\Delta CH_4/\Delta CO_2$ ratios are consistently higher than inventory estimates.
- Satellite NO_2 and HCHO enhancements co-locate with ground-based GHG hotspots, confirming key industrial sources.

ARTICLE INFO

Keywords index:
Greenhouse gases
Emission inventories
remote sensing data
Urban air quality
Houston

ABSTRACT

This study integrates in-situ and satellite observations to characterize urban greenhouse gas (GHG) emissions across Houston, Texas USA. Surface-based background concentrations show seasonal reductions from ~435 to ~410 ppm for carbon dioxide (CO_2) due to photosynthetic uptake, and from ~2.02 to ~1.88 ppm for methane (CH_4) predominantly due to oxidation by the hydroxyl radical (OH). Boundary layer height corrected excess CO_2 and CH_4 (ΔCO_2, ΔCH_4) peak in winter (~139.4 ppm, ~5.5 ppm) and drop in summer (~5.6 ppm, ~0.08 ppm), highlighting emission seasonality. The observed annual $\Delta CH_4/\Delta CO_2$ ratio (9.4 ppb ppm^{-1}) exceeds EDGAR and EPA inventory estimates by 65–70 %, and spatial mapping identifies key CH_4 hotspots - such as McCarty and Blue Ridge landfills - with ratios larger than 40–70 ppb ppm^{-1}, which are severely underrepresented in emission inventories.

Satellite-derived enhancements from OCO-3 and TROPOMI offer broader coverage but lack sensitivity to surface plumes. For example, in situ bivariate plots show sharp ΔCO_2 enhancements >30 ppm and ΔCH_4 up to ~0.3 ppm over industrial zones like the Ship Channel, while satellite ΔXCO_2 (~5–7 ppm) and ΔXCH_4 (~0.03–0.04 ppm) show moderate enhancements over the urban core. TROPOMI NO_2 (~1×10^{-4} μmol/m^2) and HCHO (~2.0×10^{-4} mol/m^2) enhancements further confirm co-located industrial emissions. This synthesis underscores the value of combining surface and satellite data for robust urban emission assessments and improved emission inventory evaluation.

1. Introduction

Climate change induced by increasing anthropogenic greenhouse gas (GHG) emissions is a major environmental issue today. Carbon dioxide (CO_2) and methane (CH_4) combined make up 98.6 % of the US GHG emissions for the year 2023 (https://www.epa.gov/ghgreporting/ghgrp-emissions-ghg). CO_2 is the most abundantly emitted GHG from anthropogenic activities and is the primary contributor to global warming, accounting for approximately 70 % of the anthropogenic influence (IPCC, 2007). It is naturally present in the atmosphere as part of the Earth's carbon cycle, which involves the exchange of carbon among the atmosphere, oceans, soil, plants, and animals.

CH_4, while less abundant than CO_2, is a significant greenhouse gas due to its high global warming potential (GWP). It is responsible for

* Corresponding author. University of Houston, Institute for Climate and Atmospheric Science, Department of Earth and Atmospheric Sciences, 4800 Calhoun Rd, Houston, TX, 77204-5007, USA.
E-mail address: ikarim2@uh.edu (I. Karim).

https://doi.org/10.1016/j.atmosenv.2025.121713
Received 21 August 2025; Received in revised form 15 October 2025; Accepted 25 November 2025
Available online 28 November 2025

approximately 20 % of the anthropogenic contribution to global warming, making it the second most important GHG after CO_2 (IPCC, 2007). The remaining contributions to global warming come from other GHGs, such as nitrous oxide (N_2O) and fluorinated gases. The GWP is a metric that quantifies the cumulative radiative forcing, considering both direct and indirect effects, over a specific time horizon (e.g., 100 years) relative to CO_2 (IPCC et al., 1990). This metric underscores the significant role of CH_4 in global warming, despite its lower atmospheric concentration compared to CO_2. Methane has a GWP which is 20 times larger than that of CO_2 over a 100-year time horizon, but has a relatively short lifetime of approximately 11.2 years, compared to CO_2, which can remain in the atmosphere for 1000 years (Ciais et al., 2013; East et al., 2024). The overall effect of the shorter lifetime and large infrared absorption is reflected in the GWP. The CH_4 GWP also accounts for indirect effects, such as CH_4 being a precursor to ozone, which itself is a GHG (EPA, 2022).

Sources of CO_2 and CH_4 emissions include both natural processes and human activities. However, the increase in atmospheric CO_2 since the industrial revolution is primarily driven by human-related activities such as fossil fuel combustion and deforestation. While deforestation reduces the capacity of forests to act as carbon sinks, it also directly contributes to emissions through the burning or decomposition of biomass, amplifying the rise in atmospheric CO_2 (IPCC, 2013). In 2020, CO_2 accounted for about 79 % of all U.S. GHG emissions from human activities (EPA, 2021). Over 70 % of the global anthropogenic CO_2 emissions originate from cities as reported in an earlier report (United Nations, 2011), but might have even increased due to continued urbanization. The magnitude of urban CO_2 emissions can be detected by elevated concentrations in so-called urban CO_2 domes (Idso et al., 1998; Kort et al., 2012; McKain et al., 2012; Pataki et al., 2003; Rice and Bostrom, 2011; Rigby et al., 2008). The CO_2 emission into the atmosphere from anthropogenic sources originates mainly (75 %) from fuel combustion (coal, oil, gas), but also from other kinds of activities (cement production, flue gas burning), making altogether 20 billion metric tons yr^{-1} (Pegov, 2008). According to Wang (2020) about 4.1 billion metric tons of cement is manufactured globally every year, which accounts for 8–10 % of anthropogenic CO_2 emissions globally, and is anticipated to continually increase in the future. During cement manufacturing CO_2 is produced in the calcination process (Worrell et al., 2001).

Plants interact with atmospheric CO_2 through their metabolism process. Through photosynthesis they absorb atmospheric CO_2 and utilize it for their growth. Through respiration plants also emit CO_2. However, during daytime the absorption of CO_2 prevails. Plants have different metabolism types. Plants whose photosynthetic pathway results in a three-carbon compound (glyceraldehyde-3-phosphate) are called C_3 plants (Ramachandran Nair, 2013), whereas C_4 plants have a supplementary carboxylation reaction which results in four-carbon compounds (oxaloacetic acid and malic acid). The Crassulacean acid metabolism (CAM) is a form of photosynthesis in which plants fix carbon at a higher water-use efficiency compared to the ancestral C_3 photosynthesis (Messerschmid et al., 2021).

Human activities are altering the carbon cycle, both by adding more CO_2 to the atmosphere and by influencing the ability of natural sinks, like forests and soils, to remove CO_2 from the atmosphere and store CO_2. Photosynthesis and transfer of CO_2 from the atmosphere into vegetative pools through green plants as well as ocean uptake absorbs large fraction of the CO_2 emissions. Oceanic uptake is about 2.2 Pg C/year, and terrestrial sinks absorbed a total of 2.7 Pg C/year during the 1990s, and 3.2 Pg during 2000s. Thus 57 % of the 9.5 Pg C emitted was absorbed by natural sinks (Lal, 2013).

Atmospheric CH_4 can be attributed to thermogenic, biogenic, and anthropogenic sources (IPCC et al., 2014). In the U.S., major anthropogenic contributors include natural gas and petroleum systems (32 %), enteric fermentation (27 %), landfills (17 %), manure management (9 %), and coal mining (6 %) (EPA, 2021). Natural emissions arise primarily from wetlands, termites, and geological seeps, with wetland fluxes peaking under anaerobic conditions and declining during drought. In contrast, CO_2 fluxes from wetlands reflect a dynamic balance between photosynthetic uptake and aerobic respiration, which can temporarily convert wetlands from sinks to sources (Hassett et al., 2024). The primary atmospheric sink for CH_4 is oxidation by hydroxyl radicals (OH), which controls its global lifetime of 11.2 years (Atkinson and Arey, 2004; East et al., 2024).

Previous studies either focused on CO_2 or CH_4, or they either used ground-based or satellite-borne data. This study performs an integrated analyses of urban and industrial CO_2 and CH_4 emissions, combining in-situ measurements and high-resolution satellite-based observations of CO_2 and CH_4. It aims to characterize anthropogenic, thermogenic, and biogenic sources in the Houston, Texas, area, a complex environment influenced by urban, industrial, and natural factors, but also serving as an almost ideal testbed for satellite remote sensing data due to its rather isolated location (no larger urban agglomeration within a radius of at least 250 km, see Fig. 1) surrounded by continental and marine environmental conditions. Unlike previous studies, this work incorporates both surface-based and remote sensing data to identify emission hotspots and their correlations with other trace gases like NO_2 indicative for different emission sources and/or chemical transformation processes. By integrating temporal (diurnal and seasonal) and spatial analyses, the study provides enhanced understanding of emission dynamics in an urban-industrial setting. While the combined satellite-surface based comparison data sets are confined to limited daytime satellite overpass time windows, the in-situ surface measurements extend the analysis to continuous temporal anatomy view over the Houston metropolitan area considering daytime variations. The combination of these datasets allows for more detailed mapping and analysis, as each of these datasets offer specific insights, for instance in-situ measurements reveal detailed diurnal variations, wheras satellites provide broad spatial coverage. Together, they enable more comprehensive and detailed mapping than using either dataset alone.

Houston stands out as one of the most complex urban environments in the U.S. due to its diverse and extensive emissions sources (Fig. 1). As the fifth-largest U.S. metropolitan area, and unlike the top three metropolitan areas New York, Los Angeles, and Chicago, which show a decrease in population, Houston shows a strong population growth which parallels with Dallas, the fourth largest metropolitain area in the U.S. (United States Census Bureau, 2025).

Houston experiences significant urban emissions, including non-methane hydrocarbons (NMHCs), nitrogen oxides (NO_x), sulfur dioxide (SO_2), particulate matter (PM), and other pollutants originating from both mobile and stationary sources. Beyond these typical urban emissions, Houston is unique due to its vast and complex industrial landscape, which includes one of the largest concentrations of petrochemical facilities in the world. This industrial sector contributes significantly to GHG emissions and air pollutants, with overlapping sources in both time and space. Previous studies have highlighted the complexity and transient nature of Houston's emissions for various compounds, such as volatile organic compounds (VOCs) (Leuchner and Rappenglück, 2010; Czader and Rappenglück, 2015; Sadeghi et al., 2022), particulate matter (Ahmed et al., 2021), and nitrophenols (Ahmed et al., 2023).

Methane is an yet relatively understudied component of Houston's emissions. While studies such as Sanchez et al. (2018) have provided valuable insights into CH_4 emissions from leaks in natural gas distribution systems in Houston residential areas Yang et al. (2019) focused on individual CH_4 sources, including landfills and petrochemical sites. These efforts have been sporadic, campaign based rather than comprehensive, longer-term measurements. They did not report enhancement values, due to the limitations of mobile measurements which would not allow for concurrent upwind vs downwind measurements. Even more concerning is the complete absence of systematic CO_2 observations across the region. This critical data gap severely hinders our ability to quantify total carbon related GHG emissions. Without longer-term,

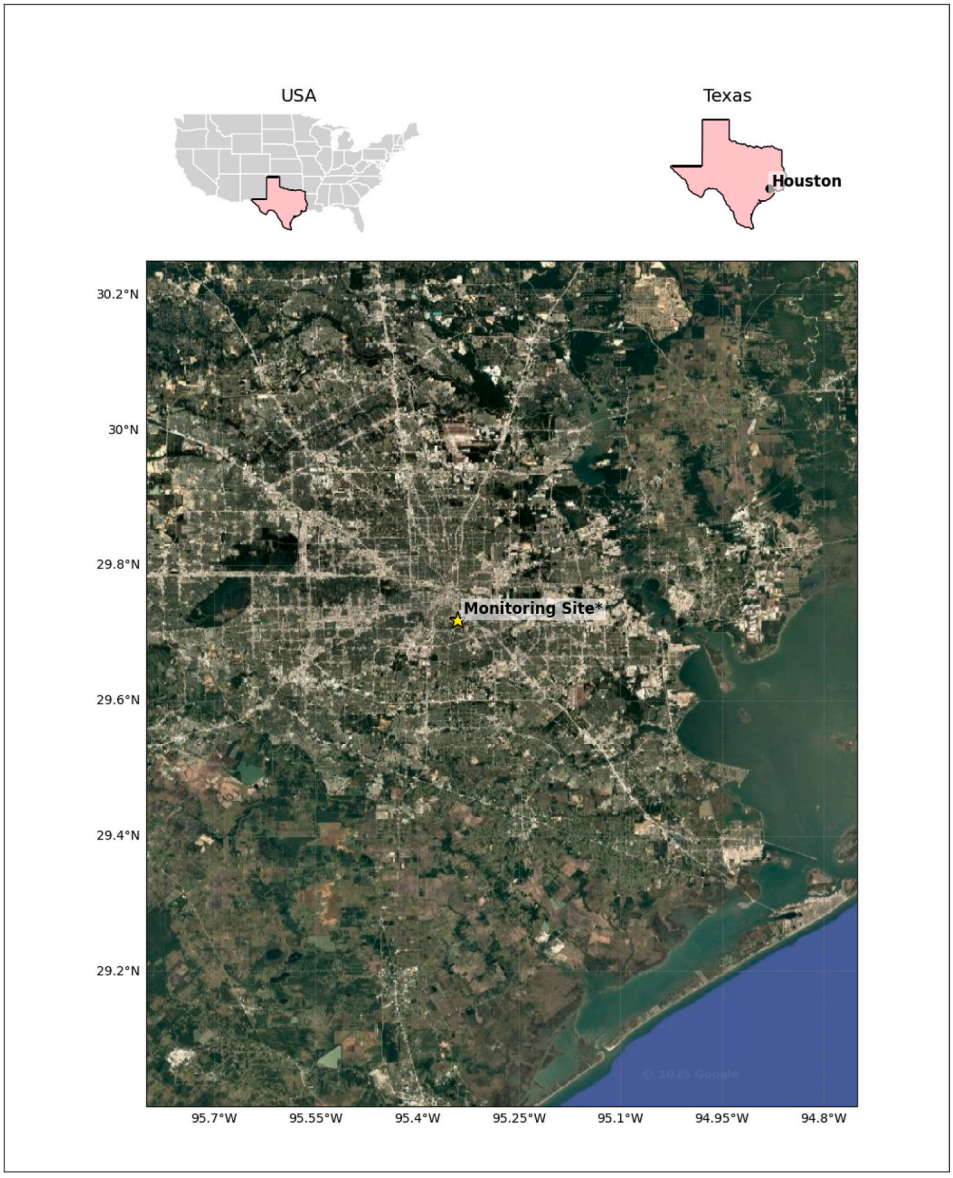

Fig. 1. Map of the United States with the state of Texas (Top) and Zoomed in satellite view of the Houston with the monitoring site marked by a yellow star.

city-scale CO_2 observations, efforts to validate emission inventories remain fundamentally incomplete. In contrast, our study provides a spatially continuous, longer-term assessment of CH_4 and CO_2 data concurrently taken using both ground-based networks and satellite data. We emphasize temporal trends, co-pollutant relationships, and boundary layer corrections, enabling broader emission diagnostics beyond isolated source plumes.

Geographically, Houston is largely surrounded by low-population-density areas with minimal industrial activity and urban infrastructure. These surrounding regions, dominated by Texas coastal prairie ecosystems, including hay pastures, forests, and wetlands (Statkewicz et al., 2021), create a distinct contrast between urban and background atmospheric conditions. Additionally, the Gulf of Mexico, located south of Houston, presents a marine environment that further influences regional atmospheric dynamics. It has recently been shown that this coastal area can be used to describe atmospheric background conditions with regard non-methane hydrocarbons (Ahmed et al., 2025). This geographical setting makes Houston an ideal location for remote sensing analyses, where urban CO_2 and CH_4 domes can be detected, and emission hotspot areas can be distinguished from background conditions (Fig. 1).

Space-borne greenhouse gas measurements from instruments such as Tropospheric Monitoring Instrument (TROPOMI) and Orbiting Carbon Observatory-3 (OCO-3) provide valuable regional-scale coverage but are constrained by overpass timing and spatial resolution. TROPOMI delivers a single early-afternoon snapshot (~13:00 LST) with coarse native pixels, while OCO-3 offers targeted mapping but still depends on discrete overpasses, leaving large gaps in the diurnal record (Mastrogiacomo et al., 2025). These limitations hinder their ability to capture short-lived plumes, rapid emission changes, and complete daily variability capabilities essential for source detection and attribution in complex, multi-source environments (Liu et al., 2021). Given the complexity of emission sources and their spatial and temporal variability, a more comprehensive approach to CO_2 and CH_4 monitoring is crucial to accurately quantify emissions and assess their impact on regional atmospheric chemistry and climate. In this paper we apply a complimentary approach based on in-situ measurements which provide continuous, hourly observations that resolve the full diurnal cycle and fine-scale spatial patterns, enabling the detection of emission features often missed by satellite retrievals.

2. Data sources and methods

2.1. Surface-based in-situ measurements of CH_4 and CO_2

Here we aim to characterize anthropogenic, thermogenic, and biogenic CO_2 and CH_4 emission sources in Houston by leveraging in-situ atmospheric data collection. Our analysis is based on in-situ measurements conducted at the roof level of the Moody Tower (MT) (29.71°N, 95.34°W; 75 m above ground level) at the University of Houston (Fig. 1) from 01 January to December 31, 2022. This campus site has been in use for air quality measurements since 2006 and is well-documented (Lefer and Rappenglück, 2010). The Moody Tower is about 4 km southeast of downtown Houston. Major freeways are located 2–4 km away from MT and the Houston Ship Channel with its industrial facilities stretches over an area 10–20 km to the east of MT (Lefer and Rappenglück, 2010). The Picarro G2201-i cavity ring-down spectroscopy (CRDS) analyzer (Picarro Inc., Santa Clara, USA) was used to provide real-time measurements of CO_2 and CH_4 concentrations. Briefly, a gas sample stream is continuously pumped through a pressure (0.1947 ± 0.0002 atm) and temperature (40 ± 0.005 °C) controlled cavity, which has three mirrors to extend pathlength of traveling light wave. Light is emitted into the cavity by a continuous wave laser until a threshold is reached; then, the laser is switched off. The concentrations of CH_4 and CO_2 are determined by the decay rate (or 'ring down') of the specific spectral absorption line, which is compared to the cavity-only (i.e., without the absorbing gas) ring-down rate. The cavity only ring down rate is continuously measured using a laser tuned to a wavelength where adsorption by sample gas does not occur (Kerstel, 2004; Kerstel and Gianfrani, 2008). The PICARRO G2201-i has an accuracy of <0.005 ppm for CO_2 and CH_4 (Skorokhod et al., 2016. The Picarro G2201-i was routinely calibrated using certified methane standards (2.02 ppm and 20.16 ppm CH_4; Scott-Marrin, Inc., USA) and zero air. Since this analyzer quantifies both, CH_4 and CO_2, via infrared absorption of carbon-bearing molecules with a linear response to carbon, these CH_4 standards were also used for CO_2 calibration. Two-point calibrations showed excellent performance with slopes between 0.987 and 0.993 and offsets in the one digit ppb range, with the instrument performance remaining within the manufacturer's stated accuracy of ±200 ppb +0.05 % of the reading. Corresponding calibration curves were applied to the CH_4 and CO_2, raw data. The precision of the instrument was 0.05 % based on 15 min calibration gas sampling. The overall uncertainty is determined by the calibration with a stated uncertainty of ±1 %.

The regional concentration distributions were derived using bivariate polar plots, a statistical approach implemented via the openair package in R. Rather than generating physical imagery, this method infers spatial emission patterns by correlating time-resolved in-situ gas concentration data with wind speed and direction. By applying Generalized Additive Models (GAMs), the technique estimates directional source contributions and highlights dominant emission sectors and based on observed concentration enhancements under different meteorological conditions. This diagnostic method is widely used for visualizing potential source regions and has been validated in numerous air quality studies (Balashov et al., 2020; Carslaw et al., 2006; Henry et al., 2002; Westmoreland et al., 2007; Yu et al., 2004).

2.2. Determination of background values

The dataset was first classified into eight wind sectors based on 45° intervals Northeast (NE), East-Northeast (ENE), East-Southeast (ESE), Southeast (SE), Southwest (SW), West-Southwest (WSW), West-Northwest (WNW), and Northwest (NW). For each sector and month, the 5th percentile of CH_4 and CO_2 mixing ratios was calculated to represent background values, minimizing the influence of local emissions. This calculation was performed only for subsets where the number of available data points was >5. To obtain a representative background for each month, the median of these 5th percentiles for each wind sector was determined using the formula:

$$\text{Background}_{m,w} = \text{Median}(P_5^{m,w}) \quad \text{Eq. 1}$$

where $P_5^{m,w}$ represents the 5th percentile CH_4 or CO_2 mixing ratio for each month (m) and wind sector (w), where m represents the month of the year (January to December), and w represents one of the eight predefined wind sectors (NE, ENE, ESE, SE, SW, WSW, WNW, NW).

The background allocation process first considers the month to account for seasonal variations. Within each month, background mixing ratios are assigned hourly based on the wind direction. Each hourly wind direction is mapped to one of the eight predefined wind sectors, ensuring that the allocated background values reflect both seasonal and spatial variations. The background mixing ratio, as defined in equation (1), was used to calculate the excess CH_4 or CO_2 mixing ratio (ΔC_h) for each hour (h) of 2022 as defined by the difference between the observed and background values:

$$\Delta C_h = C_{\text{observed},h} - C_{\text{background},m,w} \quad \text{Eq. 2}$$

where:

- $C_{\text{observed},h}$ is the observed CH_4 or CO_2 mixing ratio at any given hour.
- $C_{\text{background},m,w}$ is the background mixing ratios assigned for that hour, based on month and wind sector.

This method helps to localize CH_4 and CO_2 enhancements by removing the spatial and seasonal variability in background CH_4 and CO_2 in Houston which - contrary to traditional background sites which are representative for a larger homogeneous emission source area (e.g. forest, wetland) is at the interface of marine and continental air masses.

2.3. Satellite based column measurements

Satellite missions provide global measurements of the atmospheric CO_2 and CH_4, nitrogen dioxide (NO_2) and formaldehyde (HCHO). Remote sensing data is from the Sentinel-5P TROPOMI for CH_4, NO_2 and HCHO and from OCO-3 for CO_2. NO_2 is co-emitted with CO_2 when fossil fuels are combusted at high temperatures which makes it a suitable tracer for combustion related CO_2. Similarly, the fuel combustion processes in oil refinery facilities, is associated with conversion of carbon into either CO or CO_2 (Abdul-Wahab et al., 2002; Alam et al., 2025). During daytime - when TROPOMI can obtain data - most atmospheric HCHO is formed secondarily through the photochemical oxidation of CH_4 and non-methane hydrocarbons (Rappenglück et al., 2010), while a minor fraction of HCHO can be emitted directly through fossil fuel combustion (co-emitted with CO_2) throughout the day, but can become prevalent at night (Rappenglück et al., 2010; Rappenglück et al., 2013; Karim and Rappenglück, 2023).

We use fully processed Level 2 products for both CH_4 and CO_2 retrievals, which have undergone comprehensive atmospheric, surface, and instrument corrections including scattering, absorption, polarization, and bias adjustments before public release. The remote sensing satellite data was averaged for each month over the period from 01 January to December 31, 2022. Spatially, the data was averaged across the grid-cell level to capture the mean distribution while preserving spatial variability for study site. Monthly average concentrations were also calculated to align with our in-situ background estimation, which was performed on a monthly basis to ensure methodological consistency (for details, see section 3.5.1).

2.3.1. CH_4, NO_2 and HCHO (TROPOMI)

CH_4, NO_2, and HCHO were retrieved from the TROPOspheric Monitoring Instrument (TROPOMI) onboard the Sentinel-5 Precursor (S5P) satellite. TROPOMI is a passive remote-sensing instrument in a sun-synchronous orbit at ~824 km altitude, with an overpass time of approximately 13:00 local solar time over Houston. It measures HCHO

at 328.5–359 nm, NO_2 at 405–465 nm, and CH_4 using absorption features near 760 nm. The nominal pixel size is ~3.5 × 5.5 km^2 at nadir for most bands, with CH_4 retrieved at a coarser resolution of ~7 × 7 km^2.

For this study, CH_4 (reported as the column-averaged dry-air mole fraction, XCH_4) data were processed in Google Earth Engine (GEE) using the Python API within the QGIS environment. The TROPOMI Level-3 CH_4 product (COPERNICUS/S5P/OFFL/L3_CH4) was filtered over Houston (50 km buffer) for 2022 and analyzed on its native 7 × 7 km^2 grid without interpolation to preserve spatial resolution. Pixel-wise 5th percentile values represented background XCH_4, while observed XCH_4 values were taken directly from daily TROPOMI measurements. Excess CH_4 (ΔXCH_4) was calculated as the difference between observed and background values. All layers were reprojected to a common reference grid and visualized in QGIS (version 3.28.3) using consistent scales and color palettes. Monthly mean of NO_2 and HCHO fields were also derived for spatial analysis in QGIS (version 3.28.3).

2.3.2. CO_2 (OCO-3)

OCO-3 can scan extensive contiguous areas, approximately 80 × 80 km^2, during a single overpass over emission hotspots such as cities, power plants, or volcanoes. This capability is achieved through its observational modes, Snapshot Area Map (SAM) and target mode, which generate high-resolution spatial maps of XCO_2, the column-averaged dry-air mole fraction of CO_2. The OCO-3 sensor provides measurements of XCO_2 in ppm. OCO-3 crossing is roughly 13:15–13:30 local solar time. The along-track footprint size of OCO-3 at nadir is approximately 2.2 km, while the cross-track footprint size is ≤ 1.6 km, resulting in a total footprint area of about 3.5 km^2 (Eldering et al., 2019). For the present study we use XCO_2 data from the GloCE v1.0: Global CO_2 Enhancement Dataset (2019–2023) compiled by Fan et al. (2025), available via Zenodo [https://doi.org/10.5281/zenodo.15209825]. The XCO_2 data for the year 2022 was visualized using Google Colaboratory.

3. Results and discussion

3.1. Background variations of CO_2 and CH_4

Fig. 2 shows the 2022 time series of CO_2 and CH_4 mixing ratios at the monitoring site. Both gases exhibit frequent sharp spikes above background levels, indicating short-term local enhancements, superimposed on a longer-term seasonal cycle with higher concentrations in winter and lower values in summer. Background levels for CO_2 and CH_4 were derived following the procedure outlined in the previous section.

Background variability is shaped by the origin of incoming air masses and their seasonal modification by emissions and atmospheric processing. Houston's coastal location makes this more complex than at remote greenhouse-gas monitoring sites (e.g., WMO GAW; https://gawsis.meteoswiss.ch/GAWSIS/#/), as it sits at the interface of marine and continental air masses. Large-scale synoptic flows and land–sea breeze circulations (Caicedo et al., 2019; Day et al., 2010) lead to alternating marine and continental influences. Marine inflow generally lowers background levels: over the ocean, CO_2 is partly removed via dissolution, controlled by sea-surface temperature and solar radiation, which also regulate photosynthetic uptake (Le Quéré et al., 2018). CH_4 over the ocean is typically low; although some is produced in coastal sediments, most is consumed before reaching the atmosphere, except during ebullition events in stratified waters (Hermans et al., 2024). By contrast, continental air masses carry elevated CO_2 and CH_4 from anthropogenic activities, soil microbes, and vegetation. Vegetation acts as a strong CO_2 sink through photosynthesis during the growing season, while respiration (Beer et al., 2010) and soil microbial processes supply CO_2 and CH_4, both enhanced under warm, moist conditions.

The seasonal drawdown of CO_2 from a winter maximum (~435 ppm) to a summer minimum (~410 ppm) reflects photosynthetic uptake exceeding respiration during spring and summer (Mavrovic et al., 2023). In parallel, CH_4 levels decline from ~2.02 ppm in winter to ~1.88 ppm in summer (Fig. 2). As discussed in the Introduction, CH_4 lacks a terrestrial sink, and its only significant removal is oxidation by OH radicals (Atkinson and Arey, 2004). Assuming an average OH concentration of 5.0 × 10^5 molecules cm^{-3} and a reaction rate constant kOH of 6.4 × 10^{-15} cm^3 $molecule^{-1}$ s^{-1}, this OH-driven sink explains the observed summertime decline. The amplitude of the seasonal change is larger than at remote sites (East et al., 2024), likely due to Houston's latitude, which favors strong OH loss in summer, and its coastal setting, which limits the seasonal enhancement from continental wetlands.

Overall, background CO_2 and CH_4 mixing ratios ranged from ~410

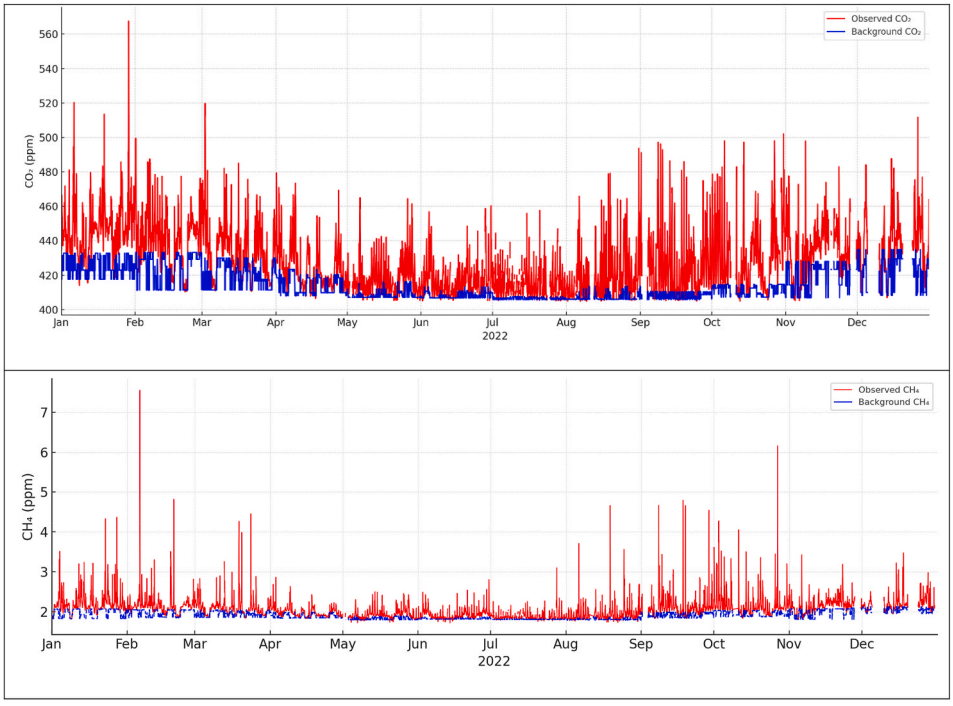

Fig. 2. Observed and background CO_2 (top) and CH4 (bottom) time seriess for 2022.

ppm to ~1.85 ppm in southern, marine-influenced sectors to >435 ppm and 2.05 ppm in northern, continental sectors (Fig. 3). Annual background averages (414.5 ppm for CO_2, 1.91 ppm for CH_4) closely match the global means for 2022 (417.9 ± 0.2 ppm CO_2, 1.923 ± 0.002 ppm CH_4; WMO, 2023).

3.2. Temporal variation of boundary layer height corrected ΔCO_2 and ΔCH_4

The diurnal variation of the boundary layer height (BLH) modulates the surface mixing ratios of air pollutants (Akther et al., 2023), as well as greenhouse gases, as it is has been shown for CO_2, for instance (Newman et al., 2013). Removing the effect of the BLH variation removes accumulation or dilution processes due to vertical atmospheric mixing, respectively. In this scenario, ΔCO_2 and ΔCH_4 values would predominantly reflect gas exchange processes assuming chemical and deposition removal processes would be negligeable, which is a reasonable assumption for CH_4 and CO_2 on diurnal time scale. To account for the influence of boundary layer height (BLH) on ΔCO_2 and ΔCH_4 concentrations, we applied a diurnal normalization based on CH_4 observations. Contrary to CO_2, whose diurnal ambient concentrations are modulated by seasonal-dependant light-driven diurnal variation of biogenic activity, which include emissions and absorption, background biogenic CH_4 emission sources are predominantly temperature-driven and thus have less impact on ambient concentrations on a diurnal scale than it is the case for CO_2. Also, the atmospheric lifetime of about 11.2 years for CH_4 is significantly longer than the time-scale of diurnal BLH variations. In the absence of short-term emissions on a time-scale less than a day, e.g. in remote regions, the diurnal variation of CH_4 concentrations would largely reflect the diurnal variations of the BLH (e.g. see Kavitha et al., 2018). For an urban area we would assume the addition of fluctuating anthropogenic CH_4 emission sources throughout the day (in contrast to CO_2, which would also be associated with recurrent anthropogenic sources, such as traffic rush hours as shown by Rappenglück et al., 2013 for the Houston case). In Appendix A of the supplementary material we elaborate on the use of CH_4 data as a proxy for BLH.

For each month, CH_4 observations were grouped by hour (0–23), and hourly medians were calculated. This monthly approach was chosen to better reflect the seasonal variation in diurnal boundary layer dynamics, as BLHs largely depend on the strength of surface heat fluxes and these in turn are impacted by the variation of incoming solar energy (for some BLH analysis in the Houston area see Caicedo et al., 2019; Cuchiara and Rappenglück, 2018; Li and Rappenglueck, 2018; Wilmot et al., 2014, and references therein). Grouping by month yields about 30 data points for each hour which represents a statistical sound basis for calculating medians and minimizing potential outlier effects. Dividing each hourly median by the peak 24 hourly median yielded a normalization factor for each hour. This factor was then applied to the hourly ΔCH_4 and ΔCO_2 values to yield $\Delta CH_{4(BLHcorr)}$ and $\Delta CO_{2(BLHcorr)}$ to correct for diurnal dynamic effects due to BLH variability according to the following equations:

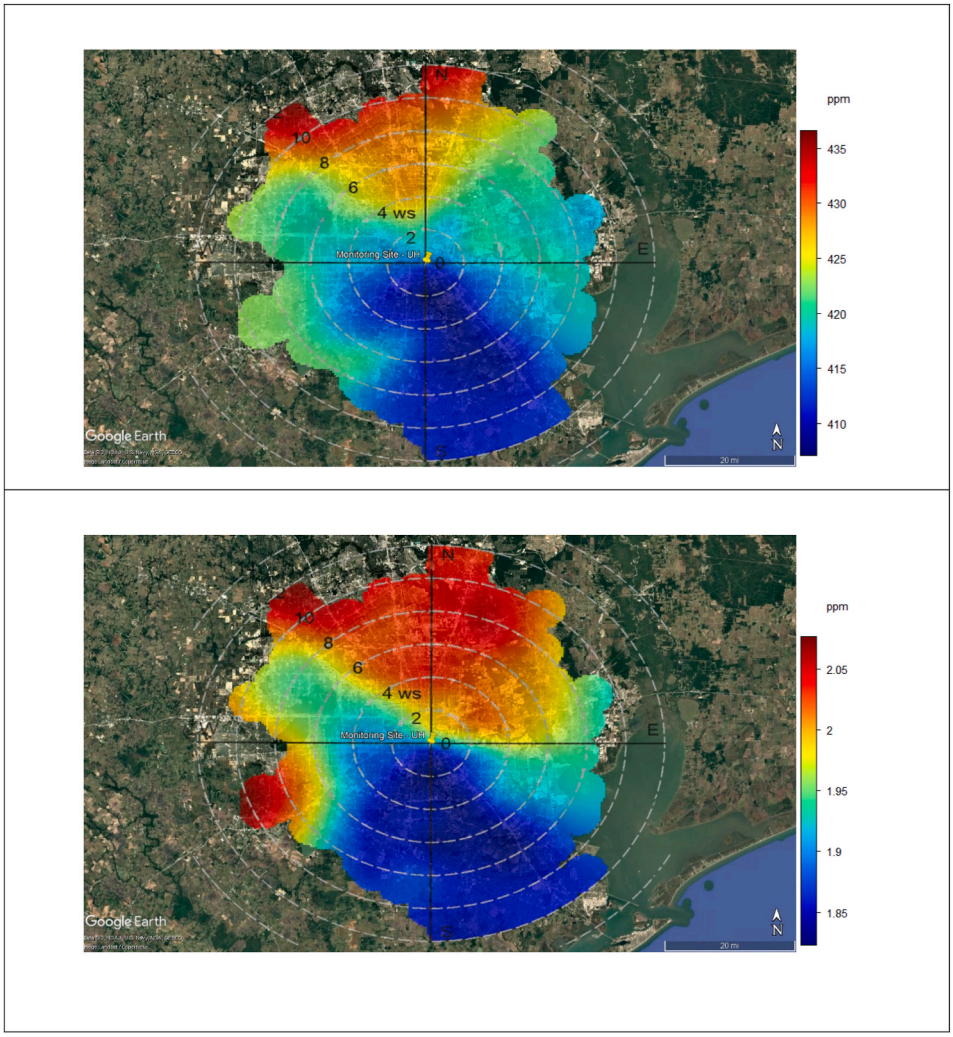

Fig. 3. Background bivariate plot for CO_2 (top) and CH_4 (below) mixing ratios calculated as arithmetic means over 2022.

$$\Delta CO_{2,BLH_{corrected}}(t,h_d) = \Delta CO_2(t,h_d) \cdot \frac{\max(median(CH_4(d_m)))}{median(CH_4(h_d))} \quad \text{Eq. 3}$$

$$\Delta CH_{4,BLH_{corrected}}(t,h_d) = \Delta CH_4(t,h_d) \cdot \frac{max(median(CH_4(d_m)))}{median(CH_4(h_d))} \quad \text{Eq. 4}$$

where t is any timestamp in the time series of ΔCO_2 and ΔCH_4, and h_d is the timestamp 0 … 23 of the median monthly diurnal variation d_m.

Fig. 4 shows pronounced seasonal variation of BLH corrected ΔCO_2 throughout 2022, with the highest enhancements early in the year from January through March. During this period, ΔCO_2 frequently exceeded 50 ppm, with peak values reaching up to ~139 ppm. Monthly mean ΔCO_2 falls from ~11.6 ppm in April to a summer low of ~9.5 ppm in July, then rebounds to ~15.2 ppm in August. It climbs further to ~19.7 ppm in September and reaches a maximum of ~22.3 ppm in October, before declining to ~17.5 ppm in November and edging up to ~18.5 ppm in December. These seasonal patterns and the remaining month-to-month variability therefore reflect the rise and fall of anthropogenic CO_2 sources. To further contextualize these observational patterns, Fig. S2 illustrates the seasonal variability of near-surface CO_2 in Houston. The top panel shows daily BLH-corrected ΔCO_2 enhancements for 2022, which exhibit clear seasonal patterns highest in winter and early spring, with large day-to-day variations frequently exceeding 40 ppm, then declining to a minimum (5–10 ppm) in summer with dampened day-to-day variations before rising again in late autumn (20–30 ppm). The bottom panel depicts anthropogenic CO_2 emissions from the year 2021 along with their sectoral contributions, which is the most recent available year from the Carbon Monitor Cities platform (https://cities.carbonmonitor.org/; Huo et al., 2022). These emissions include residential, industrial, and ground transport sectors. We did not include the power generation sector, as major facilities like the Parish power plant lie outside the urban boundaries defined by the bivariate plot in Fig. 4. We did not include the aviation emissions neither for two reasons: still, during the year 2021 aviation activity continued to be on the rise to

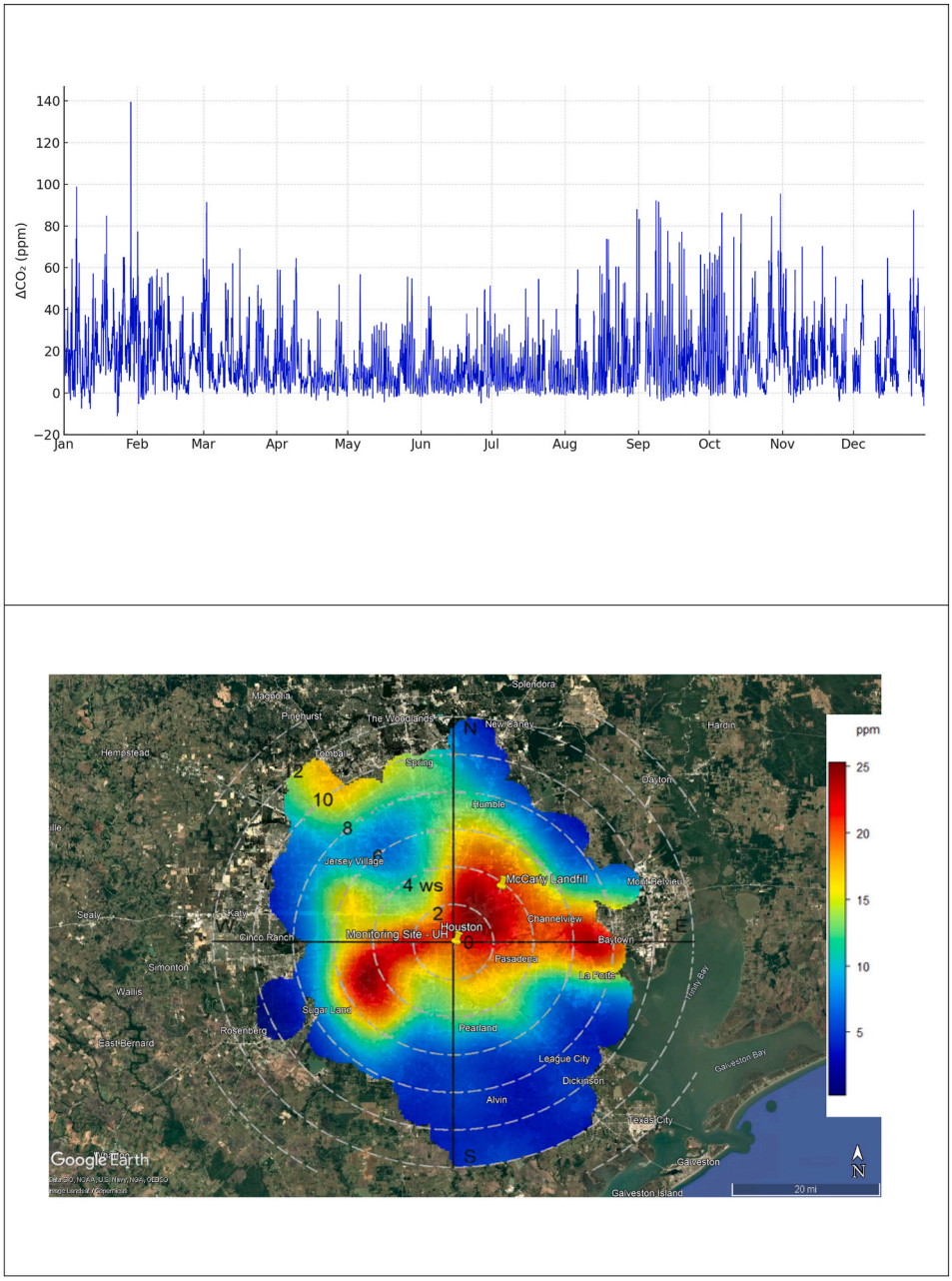

Fig. 4. Time series (top) and bivariate plot (below) for BLH corrected ΔCO_2 calculated as arithmetic means over 2022.

levels before the drastic COVID-19 reductions and also, its contribution – mainly confined to the airport activities – did not exceed 5 % of the combined residential, industrial, and ground transport sectors at any time. According to the Air Alliance Houston Climate Action Plan (2022), CO_2 emissions from point sources in Houston include petrochemicals, petroleum product suppliers, and refineries (together ~38 %), power plants ~28.2 %, chemical industry 24.9 %, and other stationary sources (industrial gas suppliers, waste facilities, minor sectors) collectively <10 %. The industrial and ground transport sectors exhibit some seasonal variations with higher (for the industry) and lower (for the ground transport) emissions in wintertime, whereas both would show rather consistent levels of similar magnitude in other seasons. The residential sector displays some pronounced seasonal variation with consistently low levels during the summer until early fall, whereas in other times emissions significantly increase and show strong day-to-day variations which clearly dominate the time series of the combined emission sectors (upper panel of Fig. S2). These strongly varying amplitudes are also distinguishable in the observation of the BLH-corrected ΔCO_2 enhancements, which would indicate the prevalence of the same emission, i.e. residential emissions. The fractional breakdown reveals that industry contributes around 40–50 % of Houston's daily CO_2 emissions. The contribution from ground transport varies from 30 to 40 %, with largest contribution during the summer. In contrast, residential emission shares rise sharply in winter up to ~30 % due to increased heating demand and would fall to 10 % in summertime. These patterns in Houston's emissions and near-surface ΔCO_2 are consistent with the sectoral contributions and seasonal trends observed by Huo et al. (2022) across other major cities, emphasizing that industrial activity and increased residential heating during winter are primary drivers of urban CO_2 seasonality. The inclusion of Huo et al.'s (2022) sector-resolved emission estimates in Fig. S2 provides context for interpreting our 2022 in-situ ΔCO_2 observations, using the most recent sectoral breakdown for Houston Climate Action Plan (2022). This comparison highlights the strength of our BLH-corrected approach, which captures the full diurnal cycle and resolves both spatial temporal variations, unlike satellite products such as TROPOMI that are limited to a single early-afternoon overpass (~13:00 LST). This makes our method more effective for detecting and attributing seasonal patterns.

Fig. 5 exhibits a broadly similar seasonal cycle for BLH-corrected ΔCH_4, though shaped by different processes. Hourly mean BLH-

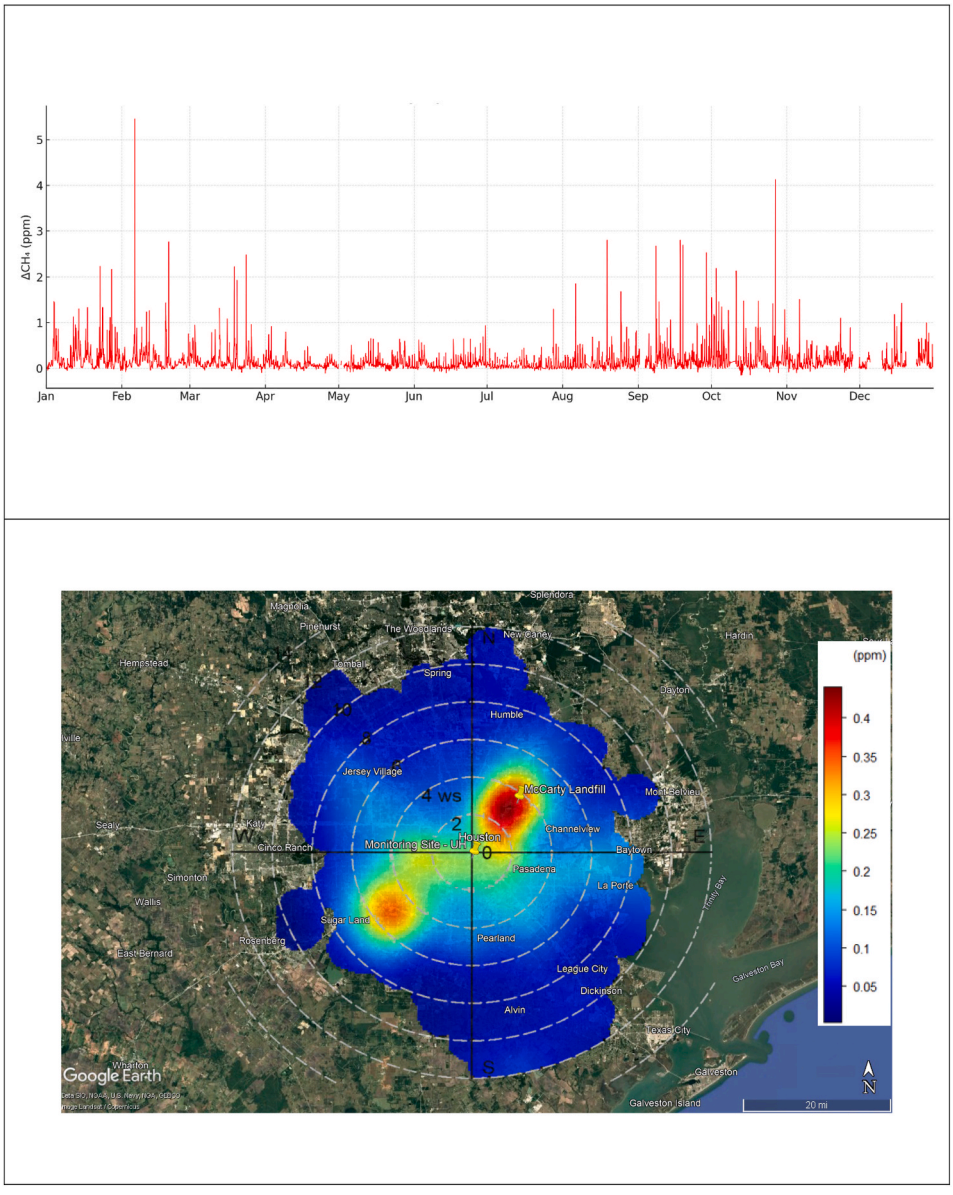

Fig. 5. Time series (top) and bivariate plot (below) for BLH corrected ΔCH_4 calculated as arithmetic means over 2022.

corrected ΔCH_4 peaks mainly in late winter to early spring (February–March) and again in early autumn (September–October), with hourly maxima reaching up to ~5.6 ppm. As spring transitions to summer, ΔCH_4 declines from ~0.11 ppm in April to a minimum of ~0.09 ppm in July, then rebounds to ~0.16 ppm in August. Concentrations continue to rise through autumn, reaching ~0.25 ppm in September and ~0.26 ppm in October, before tapering to ~0.20 ppm in November and December. Unlike CO_2, for which daily urban emission inventories for specific emission sectors have been developed (Huo et al., 2022), we are not aware of comparable CH_4 inventories for Houston. However, existing estimates suggest emissions are overwhelmingly dominated by the waste sector (78 %), with additional contributions from refineries and other industrial sources (Air Alliance Houston, 2022). Because landfill related CH_4 originates primarily from microbial processes operating year-round, emissions are relatively steady and not strongly seasonal. Instead, much of the observed variability arises from episodic "transient" events such as leaks, venting, and flaring. This sectoral profile helps explain why BLH corrected ΔCH_4 exhibits more modest seasonal variations than BLH corrected ΔCO_2, despite the expectation that higher summertime microbial activity could modestly elevate landfill emissions.

3.3. Spatial variations of BLH corrected ΔCO_2 and ΔCH_4

The BLH corrected bivariate ΔCO_2 and ΔCH_4 maps (Figs. 4 and 5) reveal the spatial distribution of ΔCO_2 and ΔCH_4 concentrations across the Houston area, highlighting distinct emission processes. ΔCO_2 dominated emissions originate primarily from combustion-related activities, such as fossil fuel burning in traffic, industrial facilities, and power plants, where carbon containing species are ultimately oxidized to CO_2. In contrast, ΔCH_4 dominated emissions are associated with fugitive or anaerobic processes, including landfills, wetlands, and wastewater treatment plants, where organic matter decomposes under oxygen-limited conditions, produce CH_4 as a primary byproduct (Kuwayama et al., 2019). Additionally, co-emission processes such as oil and gas operations or landfill sites can release both gases simultaneously at different strengths. This distinction between oxidized (CO_2) and reduced (CH_4) carbon sources provides the framework for interpreting different spatial emission patterns.

The spatial distribution of ΔCO_2 across the Houston (Fig. 4) reveals three dominant enhancement zones corresponding to key anthropogenic emission sectors. The hotspot located in the eastern portion of the domain, encompassing areas such as Galena Park, Channelview, Deer Park, Pasadena, and Baytown. This region aligns with the Houston Ship Channel, a major industrial corridor characterized by dense clusters of petrochemical facilities, oil refineries, and energy infrastructure. The elevated ΔCO_2 in this area, exceeding 20 ppm in places, is primarily attributed to continuous combustion processes, flaring, industrial fuel use and transport-related emissions. A second hotspot is over downtown Houston, reflecting emissions from high-density urban activity including traffic, building energy consumption, and commercial combustion. To the west and southwest, enhanced ΔCO_2 levels extend through Bellaire, Missouri City, and Sugar Land, by commuter traffic and transport-related emissions along major roadways such as TX-69 and Beltway 8. Outside these core zones, ΔCO_2 values decline toward the periphery of the domain, where lower population density and fewer emission sources.

The spatial distribution of ΔCH_4 reveals two dominant hotspots (Fig. 5). The strongest CH_4 enhancement is observed over the McCarty Road Landfill, with ΔCH_4 values peaking around 0.3–0.4 ppm - approximately two to three times higher than the surrounding urban areas, which show enhancements in the range of 0.1–0.15 ppm. The McCarty Road Landfill ranked 10th out of 201 based on waste accumulations in Texas (MIT Climate, 2025). A secondary CH_4 hotspot is observed to the southwest over Sugar Land, Texas - an area historically characterized by sugarcane plantations along the Brazos River floodplain. Today, Sugar Land is a rapidly expanding suburban region that still contains extensive wetlands and shallow lakes, which likely contribute to localized biogenic methane emissions (https://fwsprimary.wim.usgs.gov/wetlands/apps/wetlands-mapper/). Potential additional emission sources may include natural gas leaks. Sanchez et al. (2018) found clusters of elevated CH_4 levels impacted by biogenic and thermogenic CH_4 located in the central, west and soutwest regions of Houston, albeit with some significant spatial heterogeneity. While Sanchez et al. (2018) report campaign-based localized measurements, Fig. 5 reflects conditions averaged over the entire year and may likely reflect a merge of these sources. ΔCH_4 levels outside the urban core continuously drop below 0.01 ppm and become indistinguishable from background conditions.

Anderson et al. (2021) used the ratio of ΔCH_4 and ΔCO_2 to describe emission conditions for the city of Philadelphia based on Emissions Database for Global Atmospheric Research (EDGAR) and Environmental Protection Agency (EPA) emission inventories. Following their approach, we extracted and summed the total CH_4 and CO_2 fluxes over the Houston metropolitan region (28.5–31.0° N, −96.25 to −94.5° E) from the EDGAR v8.1 (2022), EPA GHGI v2 (2020) and EPA 2020, gridded datasets, respectively, and calculated inventory-based emission ratios as the ratio of the summed CH_4 and CO_2 mass fluxes (kg/s). In contrast, our bivariate spatial plots were constructed using arithmetic mean ΔCH_4 and ΔCO_2 values to capture the average spatial signal, which is a different methodology from the flux-sum approach used in the inventory comparison. Table 1 presents a compilation of CO_2 and CH_4 emission metrics for the Houston domain. Our in situ BLH-corrected $\Delta CH_4/\Delta CO_2$ ratio for the full year 2022 yields a median value of 9.4 ppb ppm^{-1}, which is approximately 25 % higher than the corresponding measurement-based ratio reported by Anderson et al. (2021) for Philadelphia. Notably, their analysis was limited to a one-month wintertime campaign, whereas our result reflects a full-year dataset. When comparing inventory-based values, Anderson et al. reported 2.0 (for their latest EPA 2020, inventory) and 2.3 (for their latest EDGAR v4.3.1 inventory from 2012) for $\Delta CH_4/\Delta CO_2$ ratios, which translated into underestimations by factors 3.9 and 3.3, respectively, when compared to observations In our case, the EDGAR v8.1 (2022) inventory-derived ratio for Houston is 5.7 ppb ppm^{-1}, and the EPA-based ratio using 2017 CO_2 and 2020 EPA CH_4 inventory is 5.5 ppb ppm^{-1}. These values are by a factor of 2.5–2.9 higher than reported for Philadelphia by Anderson et al., and might indicate improvements in the inventory, but still fall short by more than 65–70 % when compared to the measurements. Interestingly inventory estimates for CH_4 mass fluxes were 0.51 kg s^{-1} (EPA 2020) and 0.6 kg s^{-1} (EDGAR 4.31., 2012) for Philadelphia (Anderson et al., 2021), while our values for Houston ranges from 10.2 kg s^{-1} (EPA, 2020) to 7.1 kg s^{-1} (EDGAR v8.1, 2022), which is 12–20 times higher than the values for Philadelphia. Houston and Philadelphia are slightly different in population—Houston has about 20 % more people than Philadelphia according to recent Census estimates

Table 1
Comparison of CH_4 and CO_2 mass fluxes and corresponding BLH corrected $\Delta CH_4/\Delta CO_2$ enhancement ratios for Houston, derived from EDGAR v8.1 2022 and EPA (2020. 2017) inventories, and our 2022 online measurements at UH Moody Tower (UH, 2022).

Observations (UH, 2022)	ΔCH_4 (ppb)	ΔCO_2 (ppm)	$\Delta CH_4/\Delta CO_2$ (ppb/ppm)
median (arithmetic mean)	111.9 (182)	11.9 (16.1)	9.4 (11.3)
Inventory	**CH_4 Mass Flux (kg/s)**	**CO_2 Mass Flux (kg/s)**	**$\Delta CH_4/\Delta CO_2$ (ppb/ppm)**
EDGAR[a]	7.1	3402.3	5.7
EPA	10.2[b]	5227.2[+]	5.5

+)EPA, 2017 inventory.
[a] EDGAR 2022 inventory.
[b] EPA 2020 inventory.

(Population Division. March 2025). But they differ in their density with Houston being approximately 3.5 times less dense than Philadelphia (Population Division, 2025) which is an indicator for urban sprawl and a proxy for traffic volume, and economic development from 2012 until 2022 (57 % increase of the gross domestic product (GDP) in Houston vs 42 % increase GDP in Philadelphia from 2012 until 2022) with a preponderance on petrochemical industry in Houston compared with Philadelphia (U.S. Bureau of Economic Analysis, 2024). The limited agreement between top-down (ratio-based) and bottom-up (flux-based) inventories suggests that certain non-combustion sources such as landfills, anaerobic emissions, and pipeline leaks are not be fully captured in CH_4 centric emission inventories.

A very recent study by Mastrogiacomo et al. (2025) report $\Delta CH_4/\Delta CO_2$ ratios from satellite derived data for various U.S. cities. The data includes Phoenix (5.83 ppb ppm^{-1}), San Jose (6.87 ppb ppm^{-1}), Los Angeles (6.86 ppb ppm^{-1}), Minneapolis (8.35 ppb ppm^{-1}), Seattle (9.21 ppb ppm^{-1}), New Orleans (15.03 ppb ppm^{-1}), and Austin (27.55 ppb ppm^{-1}). They note the analysis was limited to cities with reliable boundary shapefiles and adequate TROPOMI coverage, with retrieval quality in some coastal locations degraded by land–water pixel mixing and fewer valid observations over water, which may be the reason why the Houston area was not included in their analysis. Our analysis adds the Houston case to this compilation and puts Houston in the middle range. This result demonstrates that our approach compares reasonably well with the satellite derived data, but has the advantage that it is based on temporally highly resolved day- and nighttime data and has the potential to resolve short-term deviations which could be used to explain the high values found for New Orleans and Austin, for instance.

Fig. 6 presents the bivariate distribution of BLH corrected $\Delta CH_4/\Delta CO_2$ ratios across the Houston domain, revealing pronounced spatial contrasts that highlight the relative contribution of major landfill sources. Only the three landfill facilities McCarty, Blue Ridge, and Coastal Plains display markedly elevated ratios, reaching values between approximately 40 and 70 ppb ppm^{-1}. These high-ratio regions clearly delineate sectors dominated by fugitive methane emissions associated with anaerobic landfill processes. In contrast, the remainder of the Houston area exhibits substantially lower ratios, generally below 10 ppb ppm^{-1}, reflecting well-mixed background or combustion-dominated air masses.

The overall areal average in Fig. 6 is close to 10 ppb ppm^{-1}, which aligns closely with the arithmetic mean of 11.3 ppb ppm^{-1} reported in Table 1. While Table 1 provides an aggregate value for the full dataset, Fig. 6 offers a sector-resolved view by partitioning the same data into discrete wind-direction and wind-speed bins. This bin-wise averaging approach enables the visualization of directional hotspots that would otherwise be obscured in domain-wide statistics. As a result, Fig. 6 effectively isolates emission plumes corresponding to key landfill sectors particularly the southwestern and southeastern quadrants encompassing Blue Ridge and Coastal Plains, where mean ratios rise to ~40 ppb ppm^{-1}, and the eastern sector containing McCarty, where mean ratios exceed 70 ppb ppm^{-1}.

Such a representation provides a more nuanced understanding of spatial source heterogeneity: it demonstrates that elevated $\Delta CH_4/\Delta CO_2$ ratios in Houston are not widespread but concentrated around specific landfill facilities. These localized enhancements underscore the strong influence of fugitive landfill emissions on the overall urban CH_4 budget and reinforce the interpretation that the highest $\Delta CH_4/\Delta CO_2$ ratios correspond to anaerobic rather than combustion-related sources.

Fig. 7 displays the gridded EDGAR CO_2 and CH_4 inventory map for Houston for the year 2022. EDGAR v8 largely reproduces the downtown CO_2 dome as seen in our BLH-corrected ΔCO_2 (Fig. 4 vs. Fig. 7), albeit with some dispersed CO_2 hotspots surrounding the urban core, there is a mismatch and underestimation of localized fugitive sources: while the McCarty landfill appears prominently in our bivariate spatial plots (Figs. 4 and 6) it is virtually absent in EDGAR's spatial inventory plot (Fig. 7). Both the EDGAR and EPA inventories underestimate the BLH corrected $\Delta CH_4/\Delta CO_2$ ratio when compared to in situ observations by approximately 65 % and 70 % respectively, as shown in Table 1.

3.4. Integrating ground-based and satellite observations for emission source characterization

3.4.1. Calculation of satellite-based ΔXCO_2 and ΔXCH_4

In order to integrate satellite borne data to our ground-based bivariate plots we used the GloCE v1.0 dataset's background-subtracted values for CO_2 (OCO-3) directly, as these already represent ΔXCO_2. For XCH_4 we calculate ΔXCH_4 from the satellite data as follows:

To determine satellite-based methane enhancements over the Moody Tower (MT) area, a 35 km radius buffer was defined around the MT. TROPOMI Level-3 XCH_4 data from 2022 were used to derive both background and excess concentrations on a pixel-wise basis. The background CH_4 for each grid cell was defined as the 5th percentile of all

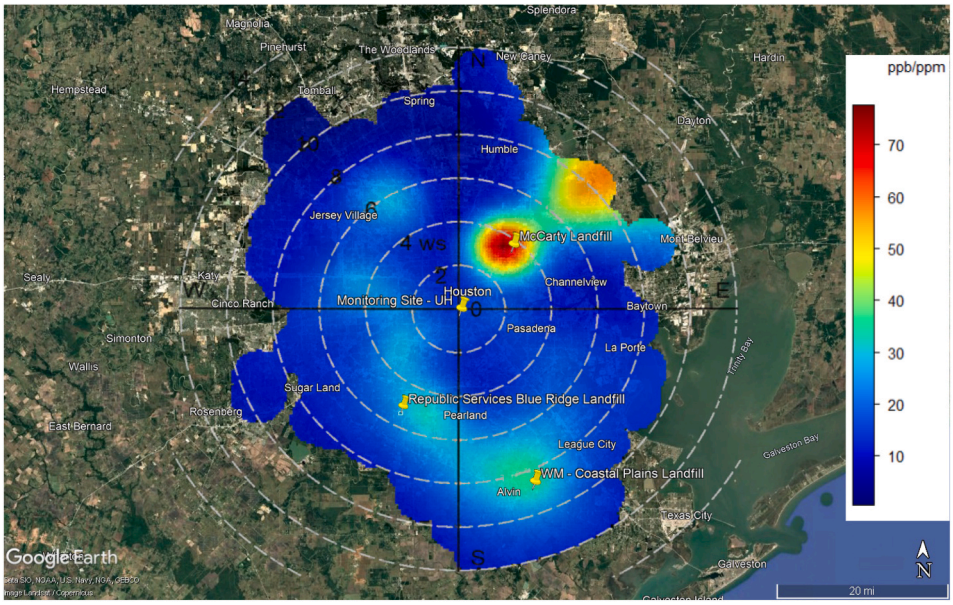

Fig. 6. Bivariate plot of BLH corrected $\Delta CH_4/\Delta CO_2$ calculated as arithmetic means over 2022.

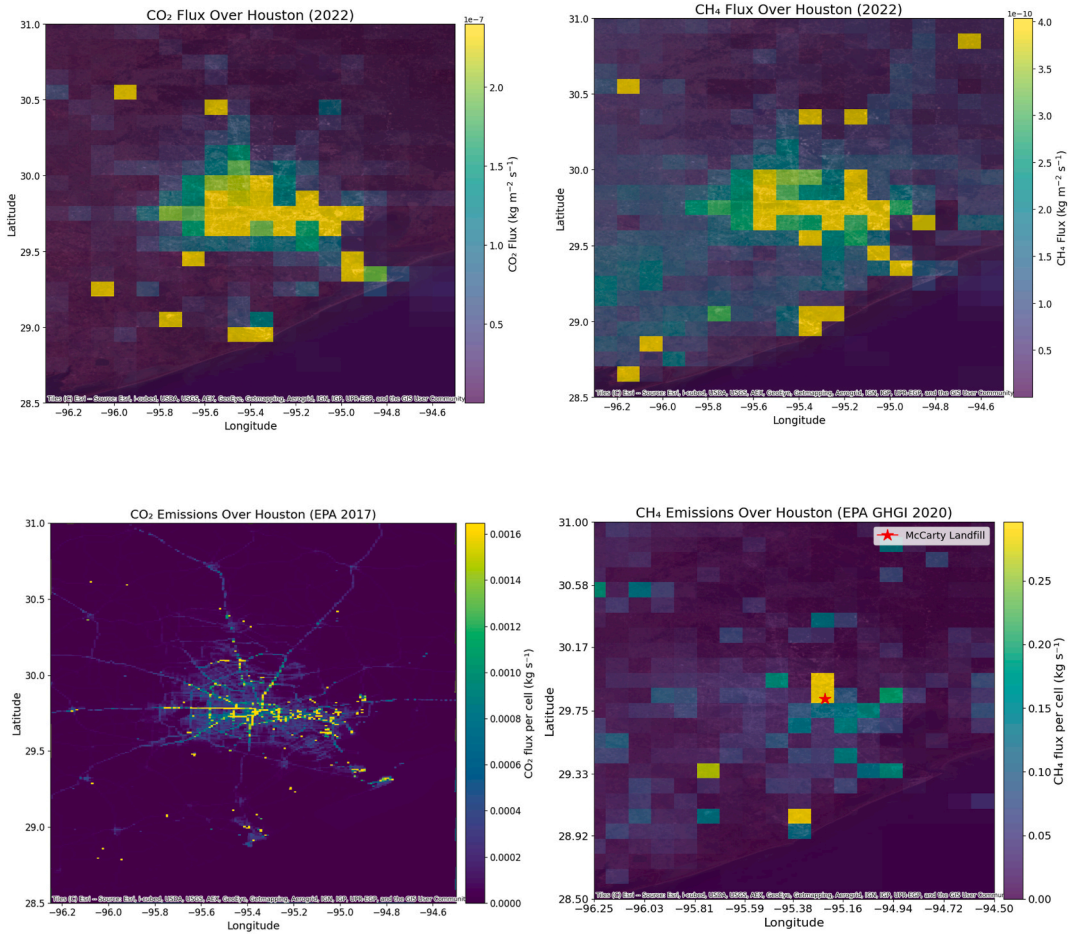

Fig. 7. EDGAR CO_2 and CH_4 flux (top) and EPA CH_4 emission over Houston (below) for 2022 (Note: the McCarty landfill site marked by a red asterisk).

XCH_4 values within the dataset, representing the lower bound of the distribution and capturing background atmospheric conditions. The observed XCH_4 was taken as the median of all available XCH_4 values per pixel, minimizing the influence of outliers and short-term variability. The excess CH_4 was then computed as the difference between the observed and background concentrations, highlighting localized methane enhancements:

$$XCH_{4,\text{background}}(i) = P_5\left(XCH_{4,\text{observed}}(i,t)\right) \quad \text{Eq. 5}$$

where P_5 denotes the 5th percentile of all observations over time t for pixel i.

The methane enhancement (ΔXCH_4) for each pixel was then computed as:

$$\Delta XCH_4(i) = \text{median}\left(XCH_{4,\text{observed}}(i)\right) - XCH_{4,\text{background}}(i) \quad \text{Eq. 6}$$

For comparison, in-situ CH_4 and CO_2 data from the MT were aggregated into a 13:00 LST bivariate polar plot, corresponding to the satellite overpass time. The in-situ and satellite datasets were aligned both spatially and temporally to the greatest extent possible; however, the ground-based measurements include all meteorological conditions, whereas satellite retrievals are restricted during cloudy periods. As a result, the TROPOMI XCH_4 record contains data gaps caused by cloud screening, retrieval filtering, and periods of satellite downtime. Specifically, no XCH_4 data were available between July 26 and August 31, 2022, due to an outage in the TROPOMI data provision system. In the following two chapters we compare the satellite XCH_4 and XCO_2 data with our ground-based data set first and then integrate satellite NO_2 and HCHO data as proxies for reactive nitrogen and VOC and their associated emission sources. As satellite measurements are confined to their overpass times we only consider bivariate plot data which aligns with the corresponding overpass time to ensure consistency in temporal sampling.

3.4.2. *CH_4: Satellite vs. surface-based bivariate plots*

As illustrated in Fig. 8, the top panel presents background CH_4 values from both the surface and satellite data. Notably, the satellite data shows some data gaps, especially close to the Bay of Galveston coast and to the North. These are usually surrounded by red pixels, which at times show some anomously steep gradients to adjacent pixels. These are most likely artifacts due to retrieval limitations which might occur in bright or humid coastal regions (land–sea mixing, sun-glint/surface-reflectance and cloud/aerosol effects), as pointed out by Mastrogiacomo et al. (2025). This may clearly affect the satellite data over the Houston area. We will not consider these areas. According to the bivariate plot, the lowest background CH_4 values (~1.85 ppm) are observed in the southern and southeastern sectors, suggesting cleaner maritime air mass impact. In contrast, slightly elevated background levels (~2.00–2.05 ppm) appear in the north and northeast, due to continental air masses with elevated concentrations of CH_4 resulting from widespread land-based sources, including anthropogenic activities and microbial processes in soils. The TROPOMI satellite-derived background XCH_4 map (Fig. 8) shows values of around ~1.90 ppm (greenish shade), with cyan shades indicating lower XCH_4 (1.88 p.m.) north and northeast of the MT within the eastern part of the urban core. The lowest values (~1.875 ppm) occur toward the southwest, with an additional low patch to the west. While the satellite XCH_4 field shows a general gradient from lower values in the surrounding suburban areas to higher concentrations

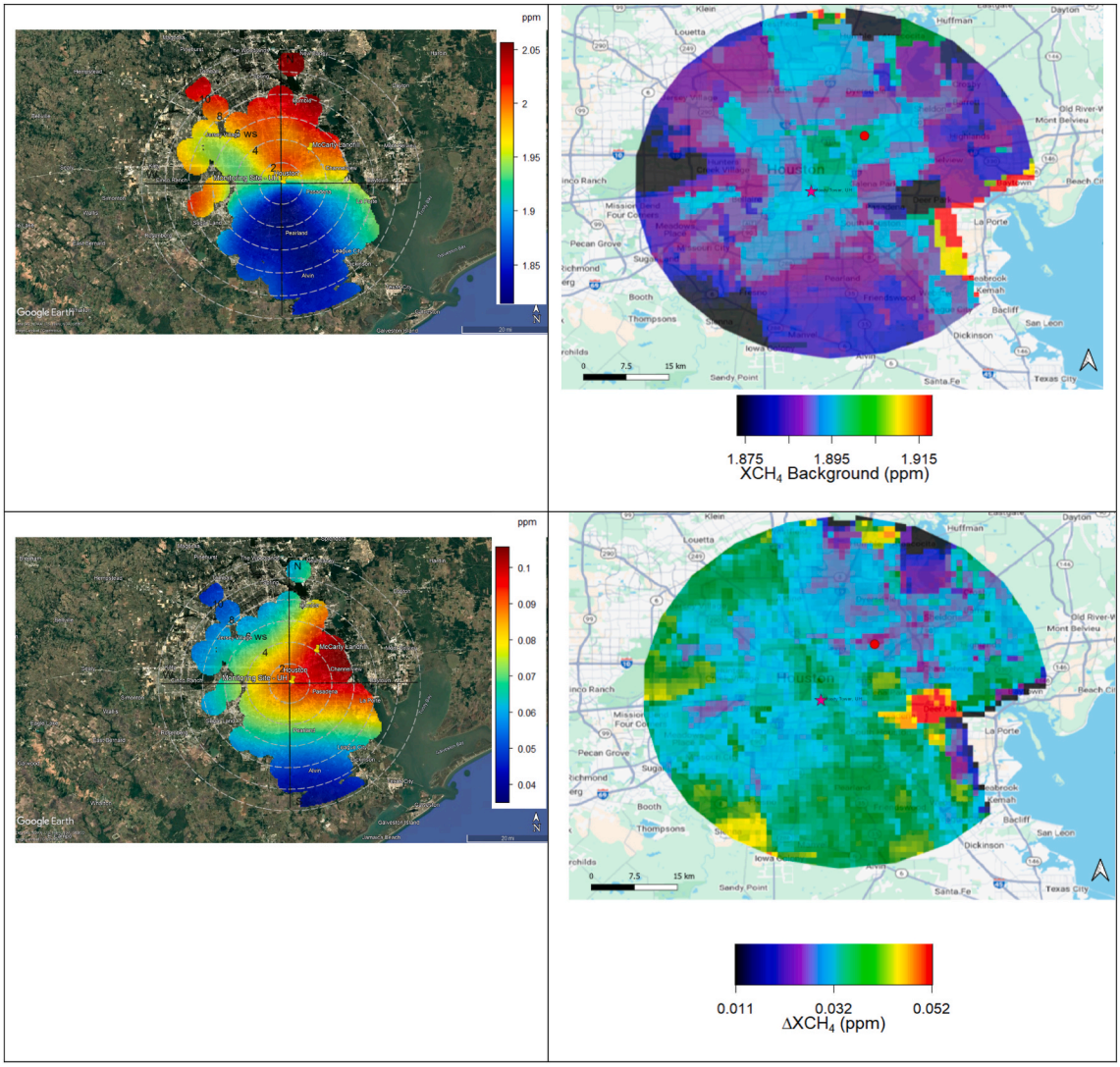

Fig. 8. Bivariate plots of background CH_4 and TROPOMI XCH_4 (top) and BLH corrected ΔCH_4 and ΔXCH_4 (bottom) at 13:00 LST for 2022. The red asterisk marks the monitoring site, and the red dot marks the McCarty Landfill.

toward the urban core, our in-situ data reveal more pronounced differences between marine and continental background air masses. Interestingly, the Ship Channel region exhibits relatively low background values, which may represent part of this transitional gradient, but this cannot be fully evaluated due to the adjacent red pixels pointing towards satellite retrieval artifacts. The red CH_4 enhancement north of MT in the surface map aligns with the cyan – green band (~1.88–1.90 ppm) seen in the TROPOMI XCH_4 data. Both datasets show lower CH_4 values toward the southeast, with the green areas in the surface map ligning up with the blueish region (~1.85 ppm) in the XCH_4 map. Although the absolute magnitudes differ, the relative pattern of elevated CH_4 compared with the adjacent southern sector is clearly consistent.

The bottom panel of Fig. 8 illustrates a comparison between surface-based BLH-corrected ΔCH_4 and TROPOMI satellite CH_4 excess for 2022 at 13:00 LST. It reveals both alignment and divergence in source attribution. The surface BLH-corrected ΔCH_4 map resolves compact, high-amplitude plumes over sources (e.g., landfill and industrial facilities), unlike the TROPOMI ΔXCH_4 data, which fails to identify these CH_4 enhancements. The surface-based plot reveals strong BLH-corrected CH_4 enhancements up to ~0.1 ppm across eastern and northeastern Houston coinciding with the McCarty landfill, major industrial and petrochemical corridors along the Ship Channel, Pasadena, and Channelview, while southern sector exhibits the lowest BLH-corrected ΔCH_4 (~0.04–0.05 ppm), with similarly low values likely extending to the west and northwest of the urban core. In contrast, the TROPOMI ΔXCH_4 field exhibits only modest enhancements, with much of the Houston domain showing greenish to bluish regions ($\leq$0.032 ppm). However, it clearly identifies a maximum ΔXCH_4 of $\approx$0.052 ppm centered over the Ship Channel. The surface-based BLH-corrected ΔCH_4 map also identifies the significantly enhanced ΔCH_4 over the Ship Channel area, but in addition reveals strong enhancements over the urban core and the McCarty landfill with peaks up to ~0.10 ppm. In essence, while both, the bivariate plot and the satellite data, clearly identifies the CH_4 enhancements over the Ship Channel, the satellite fails to capture CH_4 enhancements over the urban core and does not resolve the distinct McCarty source observed in surface data.

3.4.3. *CO_2: satellite vs. surface-based bivariate plots*

The surface-based bivariate BLH corrected ΔCO_2 plot (Fig. 9) reveals strong localized enhancements exceeding 12 ppm over the northwestern and southeastern sectors of Houston, particularly near Jersey Village, Channelview, Pasadena, and La Porte. These hotspots correspond to regions of intense industrial and combustion activity, likely influenced by the Ship Channel and nearby urban traffic emissions. The enhancement patterns, derived from in situ measurements around 13:00 LST, indicate the accumulation of CO_2 under relatively stable boundary-layer

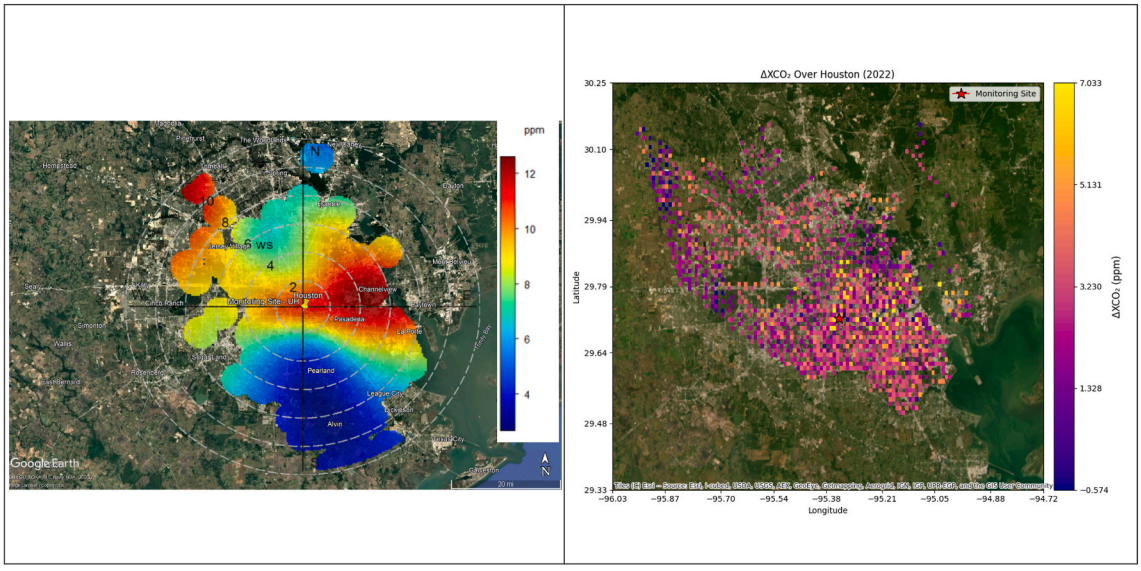

Fig. 9. Bivariate plot of BLH-corrected ΔCO_2 and OCO-3 XCO_2 at 13:00 LST for 2022, using data from the GloCE v1.0 Global CO_2 Enhancement Dataset (2019–2023) by Fan et al. (2025).

conditions. In contrast, the satellite-derived ΔXCO_2 map (Fig. 9) shows more spatially diffuse enhancements (~5–7 ppm), concentrated mainly over central and eastern Houston, including the Pasadena–Baytown–La Porte corridor. The broader spatial footprint in the satellite retrieval reflects its vertically integrated column averaging, which inherently smooths fine-scale surface gradients and reduces sensitivity to near-surface emission plumes. The EPA 2017 gridded CO_2 inventory (Fig. 7) further supports this contrast, it highlights emission corridors along highways and the Ship Channel but lacks the spatial granularity to resolve fine-scale hotspots observed in the bivariate plot. Together, these comparisons emphasize the added value of surface-based ΔCO_2 observations for identifying concentrated emission zones often under-represented in both satellite and inventory datasets.

3.4.4. *NO_2 and Co-location with ΔCH_4 and ΔCO_2*

The TROPOMI NO_2 map (Fig. 10) reveals peak tropospheric columns ($\sim 1 \times 10^{-4}$ µmol m^{-2}) over Houston's downtown–East End corridor, particularly in Pasadena and the Ship Channel, consistent with dense vehicular traffic and combustion-related emissions from petrochemical operations. These industrial sources include flaring and combustion at refineries and chemical plants. The Ship Channel area also contributes to NO_2 through marine diesel combustion, a major source of nitrogen oxides in port cities (Ramacher et al., 2020). This NO_2 hotspot spatially coincides with elevated BLH-corrected ΔCH_4 (~0.08–0.09 ppm) from the in-situ measurements, especially over the same corridor and landfill plumes to the northeast, indicating partial overlap in CH_4 and NO_2 emission signatures (Fig. 8). Importantly, the BLH-corrected ΔCO_2 map (Fig. 4) reveals a similar enhancement pattern over the Houston Ship Channel, with excess values exceeding 12 ppm, attributed to sustained industrial combustion, flaring, and transport activity. When comparing TROPOMI satellite data with our surface-based ΔCH_4 bivariate plot, we find a strong spatial alignment between ΔCH_4 and TROPOMI NO_2 enhancements over the Houston Ship Channel, highlighting this corridor as a key combustion-related emission zone. In contrast, the TROPOMI XCH_4 data fail to resolve the sharp ΔCH_4 peaks observed over Houston's major industrial and landfill areas, instead displaying a broad, diffuse enhancement northeast of the city with limited correspondence to known emission sources. Liu et al. (2021) similarly reported that while

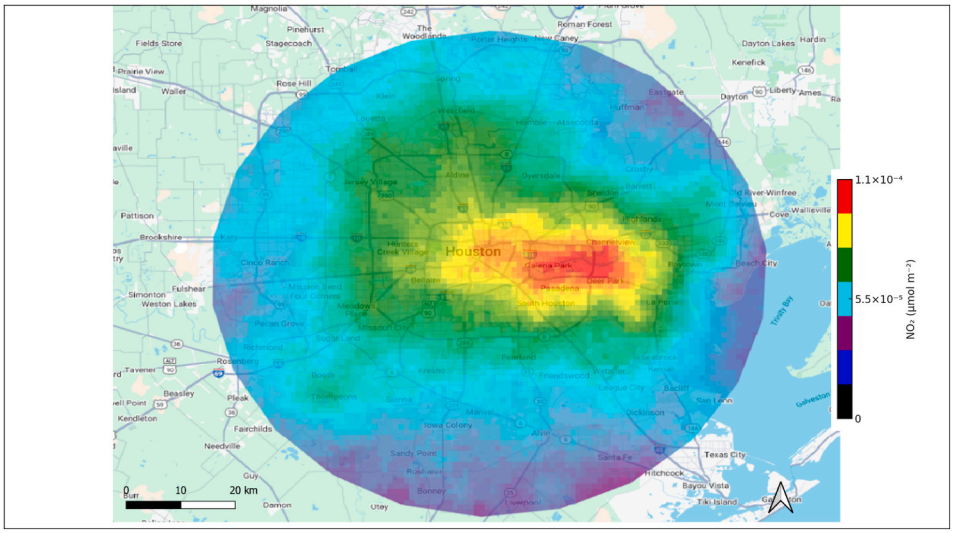

Fig. 10. NO_2 TROPOMI Satellite data at 13:00 LST for 2022.

TROPOMI retrievals effectively captured regional-scale CH_4 enhancements across Texas attributable to oil and gas production zones, livestock operations, and wetlands the signal became spatially diluted when examined at finer urban scales such as Houston. Their maps indicated scattered enhancements in the southern part of the city, which diverge from our in situ observations, and like in this study, major localized emitters such as landfills were not adequately resolved. This discrepancy underscores the limitations of current satellite CH_4 retrievals in capturing urban-industrial plumes, owing to coarse pixel resolution, a single daily overpass (~13:00 LST), and potential spatial offsets introduced by recurrent meteorological processes (e.g., land–sea breeze circulations) that influence boundary layer mixing during overpass time. Additionally, isolated high-value grid cells along domain edges likely represent retrieval artifacts from partial pixel coverage or land–water contamination and were excluded from interpretation. Despite these limitations, the co-occurrence of NO_2, ΔCH_4, and ΔCO_2 enhancements clearly identifies the Houston Ship Channel as a dominant multi-source greenhouse gas hotspot, highlighting the complementary strength of combining satellite and surface observations for robust source attribution.

3.4.5. HCHO: Photochemical and VOC emissions

The satellite-derived HCHO columns (Fig. 11) exhibit broad, diffuse enhancements across the northwest, northeast and further to the east sectors of Houston, with peak values reaching ~2.0×10^{-4} mol/m^2. The areas north of Houston have widespread forested areas, mostly composed of coniferous trees, while the southern areas are covered by coastal prairie vegetation. These elevated HCHO levels to the north reflect HCHO produced in photochemical degradation processes of biogenic VOC emissions, which can be nicely captured by TROPOMI's overpass at 13:00 local solar time, when biogenic emissions tend to reach daytime maximum. The enhanced HCHO levels to the east of Houston are associated with substantial anthropogenic contributions from industrial operations and combustion processes along the Houston Ship Channel, which can be both or primary and secondary origin (e.g. Rappenglück et al., 2010; Johansson et al., 2014b). Notably, this eastern corridor is also a key ΔCH_4 hotspot, with surface-based measurements showing peak values of ~0.3 ppm, particularly over the McCarty landfill and Ship Channel industrial area. Similarly, ΔCO_2 values in this region exceed 30 ppm, highlighting the area as a major hub of sustained fossil fuel combustion and flaring.

4. Conclusion

This study applies a methodology that bridges in-situ measurements with satellite observations to analyse CO_2 and CH_4 emission hotspots, alongside co-emitted tracers, in the Houston, Texas, area. This integrated approach improves understanding of GHG emissions in an urban–industrial environment influenced by both coastal and continental air masses.

Seasonal variations in background CO_2 and CH_4 reflect distinct biogeochemical processes. CO_2 declines from ~435 ppm in winter to ~410 ppm in summer due to photosynthetic uptake, while CH_4 decreases from ~2.02 to ~1.88 ppm mainly via OH oxidation. Background levels differ regionally, with marine-influenced sectors (~410 ppm CO_2, ~1.85 ppm CH_4) contrasting with continental sectors (>435 ppm CO_2, >2.05 ppm CH_4).

BLH-corrected ΔCO_2 and ΔCH_4 exhibit clear seasonal variability in local anthropogenic emissions. BLH-corrected ΔCO_2 shows the strongest enhancements from January to March, often exceeding 50 ppm and peaking at ~139 ppm. It decreases to a summer minimum of ~9.5 ppm in July, then rises again through autumn, reaching ~22 ppm in October before slightly declining to ~18 ppm by December. BLH-corrected ΔCH_4 peaks in late winter to early spring (February–March) and early autumn (September–October), with maxima up to ~5.6 ppm. It declines from ~0.11 ppm in April to a summer low of ~0.09 ppm in July, then rises again, reaching ~0.26 ppm in October before tapering to ~0.20 ppm by December. The 2022 mean $\Delta CH_4/\Delta CO_2$ ratio (9.4 ppb ppm^{-1}) is about 25 % higher than Philadelphia's winter in-situ value and ~65–70 % above EDGAR v8.1 and EPA estimates for Houston. Compared with recent satellite-derived $\Delta CH_4/\Delta CO_2$ ratios, Houston's citywide value falls within the mid-range of U.S. urban centers, reflecting good cross-dataset consistency. Bivariate $\Delta CH_4/\Delta CO_2$ mapping further highlights major hotspots over the McCarty, Blue Ridge, and Coastal Plains landfills (>40–70 ppb ppm^{-1}), which remain largely underrepresented in current inventories. In-situ measurements also detect sharp enhancements (~0.4 ppm CH_4; >25 ppm CO_2) at sites like the Ship Channel and McCarty landfill. Co-located satellite NO_2 peaks (~1×10^{-4} μmol m^{-2}) and HCHO enhancements (~2.0×10^{-4} mol m^{-2}) confirm the Ship Channel as a multi-source hotspot. Our BLH-corrected in-situ approach overcomes these limitations by providing continuous, high-temporal-resolution observations that capture rapid emission events and full diurnal variability, enabling more accurate detection and attribution of fine-scale sources that single early-afternoon satellite overpasses miss. It also allows the detections of plumes in the satellite sub-pixel domain.

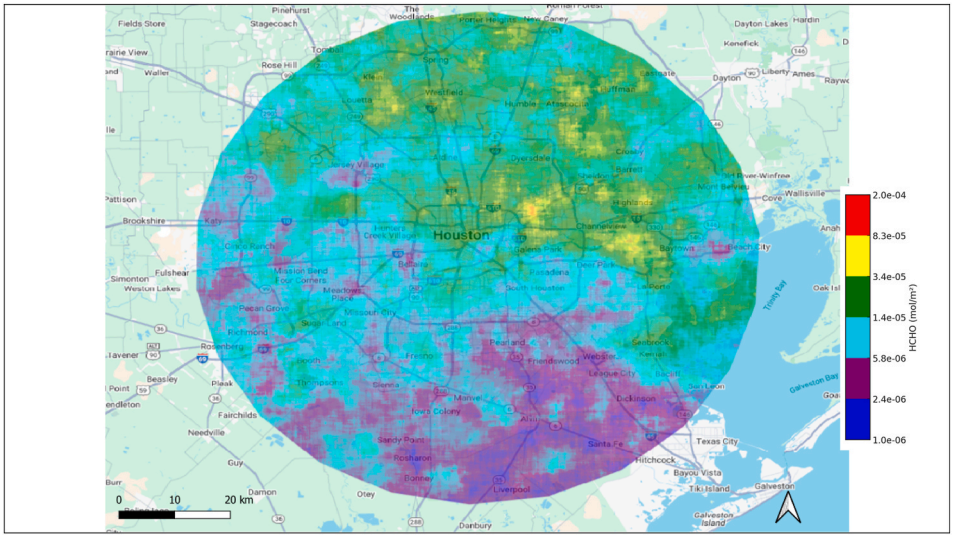

Fig. 11. HCHO TROPOMI Satellite data at 13:00 LST for 2022.

CRediT authorship contribution statement

Irfan Karim: Writing – review & editing, Writing – original draft, Visualization, Software, Methodology, Investigation, Formal analysis, Data curation, Conceptualization. **Bernhard Rappenglück:** Writing – review & editing, Validation, Supervision, Resources, Methodology, Conceptualization.

Declaration of competing interest

The author declare that they have no competing personal relationships or financial interests that could have appeared to influence the work reported in this current paper.

Acknowledgements

The authors appreciate the Copernicus program of the European Space Agency (ESA) for providing TROPOMI data on CH_4, NO_2 and HCHO. CO_2 data from the GloCE v1.0: Global CO_2 Enhancement Dataset (2022). The authors acknowledge meteorological data available made through the Texas Commission on Environmental Quality, Moody Tower C695 at UH. Irfan Karim appreciates support provided by the Higher Education Commission (HEC) of Pakistan.

Appendix A. Supplementary data

Supplementary data to this article can be found online at https://doi.org/10.1016/j.atmosenv.2025.121713.

Data availability

Data will be made available on request.

References

Abdul-Wahab, S.A., Al-Alawi, S.M., El-Zawahry, A., 2002. Patterns of SO2 emissions: a refinery case study. Environ. Model. Software 17, 563–570. https://doi.org/10.1016/S1364-8152(02)00023-3.

Ahmed, M., Ahmad, M., Rappenglueck, B., 2025. Twenty Years (2004-2023) observation of non-methane hydrocarbons in a subtropical coastal environment – indications of increased isoprene emissions. Atmos. Environ. 343, 120993. https://doi.org/10.1016/j.atmosenv.2024.120993.

Ahmed, M., Rappenglueck, B., Ganranoo, L., Dasgupta, P.K., 2023. Source apportionment of gaseous nitrophenols and their contribution to HONO formation in an urban area. Chemosphere 338, 139499. https://doi.org/10.1016/j.chemosphere.2023.139499.

Ahmed, M., Rappenglück, B., Das, S., Chellam, S., 2021. Source apportionment of volatile organic compounds, CO, SO_2 and trace metals in a complex urban atmosphere. Environ. Adv. 6, 100127. https://doi.org/10.1016/j.envadv.2021.100127.

Akther, T., Rappenglueck, B., Osibanjo, O., Retama, A., Rivera-Hernández, O., 2023. Ozone precursors and boundary layer meteorology before and during a severe ozone episode in Mexico city. Chemosphere 318, 137978. https://doi.org/10.1016/j.chemosphere.2023.137978.

Air Alliance Houston, 2022. Dirty dozen air polluters of greater Houston: 2022 report. Air alliance Houston, Houston, TX, USA. https://airalliancehouston.org/wp-content/uploads/2024/07/AAH-Dirty-Dozen-Report.pdf. (Accessed 15 August 2025).

Alam, M.J., Karim, I., Zaman, S.U., 2025. Seasonal dynamics and trends in air pollutants: a comprehensive analysis of PM2.5, NO2, CO, SO2 and O3 in Houston, USA. Air Qual. Atmos. Health. https://doi.org/10.1007/s11869-025-01790-9.

Anderson, D.C., Lindsay, A., DeCarlo, P.F., Wood, E.C., 2021. Urban emissions of nitrogen oxides, carbon monoxide, and methane determined from ground-based measurements in Philadelphia. Environ. Sci. Technol. 55, 4532–4541. https://doi.org/10.1021/acs.est.1c00294.

Atkinson, R., Arey, J., 2004. Atmospheric degradation of volatile organic compounds. ChemInform 35. https://doi.org/10.1002/chin.200410285 chin.200410285.

Balashov, N.V., Davis, K.J., Miles, N.L., Lauvaux, T., Richardson, S.J., Barkley, Z.R., Bonin, T.A., 2020. Background heterogeneity and other uncertainties in estimating urban methane flux: results from the Indianapolis Flux Experiment (INFLUX). Atmos. Chem. Phys. 20, 4545–4559. https://doi.org/10.5194/acp-20-4545-2020.

Beer, C., Reichstein, M., Tomelleri, E., Ciais, P., Jung, M., Carvalhais, N., Rödenbeck, C., Arain, M.A., Baldocchi, D., Bonan, G.B., Bondeau, A., Cescatti, A., Lasslop, G., Lindroth, A., Lomas, M., Luyssaert, S., Margolis, H., Oleson, K.W., Roupsard, O., Veenendaal, E., Viovy, N., Williams, C., Woodward, F.I., Papale, D., 2010. Terrestrial gross carbon dioxide uptake: global distribution and covariation with climate. Science 329, 834–838. https://doi.org/10.1126/science.1184984.

Carslaw, D., Beevers, S., Ropkins, K., Bell, M., 2006. Detecting and quantifying aircraft and other on-airport contributions to ambient nitrogen oxides in the vicinity of a large international airport. Atmos. Environ. 40, 5424–5434. https://doi.org/10.1016/j.atmosenv.2006.04.062.

Caicedo, V., Rappenglueck, B., Cuchiara, G., Flynn, J., Ferrare, R., Scarino, A.J., Berkoff, T., Senff, C., Langford, A., Lefer, B., 2019. Bay breeze and sea breeze circulation impacts on the planetary boundary layer and air quality from an observed and modeled DISCOVER-AQ Texas case study. JGR Atmospheres 124, 7359–7378. https://doi.org/10.1029/2019JD030523.

Ciais, P., C. Sabine, G. Bala, L. Bopp, V. Brovkin, J. Canadell, A. Chhabra, R. DeFries, J. Galloway, M. Heimann, C. Jones, C. Le Quéré, R.B. Myneni, S. Piao and P. Thornton, 2013: Carbon and other biogeochemical cycles. In: Climate Change 2013: the Physical Science Basis. Contribution of Working Group I to the Fifth Assessment Report of the Intergovernmental Panel on Climate Change [Stocker, T.F., D. Qin, G.-K. Plattner, M. Tignor, S.K. Allen, J. Boschung, A. Nauels, Y. Xia, V. Bex and P.M. Midgley (eds.)]. Cambridge University Press, Cambridge, United Kingdom and New York, NY, USA, .

Cuchiara, G.C., Rappenglück, B., 2018. Performance analysis of WRF and LES in describing the evolution and structure of the planetary boundary layer. Environ. Fluid Mech. 18, 1257–1273. https://doi.org/10.1007/s10652-018-9597-5.

Czader, B., Rappenglück, B., 2015. Modeling of 1,3-butadiene in urban and industrial areas. Atmos. Environ. 102, 30–42. https://doi.org/10.1016/j.atmosenv.2014.11.039.

Day, B.M., Rappenglück, B., Clements, C.B., Tucker, S.C., Alan Brewer, W., 2010. Nocturnal boundary layer characteristics and land breeze development in Houston, Texas during TexAQS II. Atmos. Environ. 44, 4014–4023. https://doi.org/10.1016/j.atmosenv.2009.01.031.

East, J.D., Jacob, D.J., Balasus, N., Bloom, A.A., Bruhwiler, L., Chen, Z., Kaplan, J.O., Mickley, L.J., Mooring, T.A., Penn, E., Poulter, B., Sulprizio, M.P., Worden, J.R., Yantosca, R.M., Zhang, Z., 2024. Interpreting the seasonality of atmospheric methane. Geophys. Res. Lett. 51. https://doi.org/10.1029/2024GL108494 e2024GL108494.

EDGAR v8.1 2022, Emissions Database for Global Atmospheric Research, Community GHG database version 8.1 (2023) based on data from IEA (2022) Greenhouse Gas Emissions https://edgar.jrc.ec.europa.eu/gallery?release=v2024ghg&substance=CH4&sector=TOTALS, n.d.

Eldering, A., Taylor, T.E., O'Dell, C.W., Pavlick, R., 2019. The OCO-3 mission: measurement objectives and expected performance based on 1 year of simulated data. Atmos. Meas. Tech. 12, 2341–2370. https://doi.org/10.5194/amt-12-2341-2019.

EPA 2017. ACES, Anthropogenic Carbon Emission System, 2012-2017, Version 2, https://daac.ornl.gov/NACP/guides/NACP_ACES_V2.html,n.d.

EPA 2020 Gridded GHGI version 2 – express extension dataset.https://www.epa.gov/ghgemissions/us-gridded-methane-emissions,n.d.

EPA, 2021. Overview of greenhouse gases. https://www.epa.gov/ghgemissions/overview-greenhouse.

EPA, 2022. https://www.epa.gov/ghgemissions/understanding-global-warming-potentials.

Fan, P., Liu, J., Xu, Y., Huang, B., Webster, C., Zhou, Y., 2025. A global dataset of high-resolution CO_2 enhancements derived from OCO-3 measurements. https://doi.org/10.5194/essd-2025-234.

Hassett, E., Bohrer, G., Kinsman-Costello, L., Onyango, Y., Pope, T., Smith, C., Missik, J., Eberhard, E., Villa, J., McMurray, S.E., Morin, T., 2024. Changes in inundation drive carbon dioxide and methane fluxes in a temperate wetland. Sci. Total Environ. 915, 170089. https://doi.org/10.1016/j.scitotenv.2024.170089.

Henry, R.C., Chang, Y.-S., Spiegelman, C.H., 2002. Locating nearby sources of air pollution by nonparametric regression of atmospheric concentrations on wind direction. Atmos. Environ. 36, 2237–2244. https://doi.org/10.1016/S1352-2310(02)00164-4.

Hermans, M., Stranne, C., Broman, E., Sokolov, A., Roth, F., Nascimento, F.J.A., Mörth, C.-M., Ten Hietbrink, S., Sun, X., Gustafsson, E., Gustafsson, B.G., Norkko, A., Jilbert, T., Humborg, C., 2024. Ebullition dominates methane emissions in stratified coastal waters. Sci. Total Environ. 945, 174183. https://doi.org/10.1016/j.scitotenv.2024.174183.

Houston Climate Action Plan, 2022. https://www.houstontx.gov/mayor/Resilient-Houston-Two-Year-Report.pdf.

Huo, D., Huang, X., Dou, X., Ciais, P., Li, Y., Deng, Z., Wang, Y., Cui, D., Benkhelifa, F., Sun, T., Zhu, B., Roest, G., Gurney, K.R., Ke, P., Guo, R., Lu, C., Lin, X., Lovell, A., Appleby, K., DeCola, P.L., Davis, S.J., Liu, Z., 2022. Carbon Monitor Cities near-real-time daily estimates of CO2 emissions from 1500 cities worldwide. Sci. Data 9, 533. https://doi.org/10.1038/s41597-022-01657-z.

Idso, C.D., Idso, S.B., Balling Jr., R.C., 1998. The urban CO2 dome of PHOENIX, Arizona. Phys. Geogr. 19, 95–108. https://doi.org/10.1080/02723646.1998.10642642.

IPCC, 1990. In: Houghton, J.T., Jenkins, G.J., Ephraums, J.J. (Eds.), Climate Change: the IPCC Scientific Assessment. Cambridge University Press, Cambridge, p. 410.

IPCC, 2007. Changes in atmospheric constituents and in radiative forcing. https://www.ipcc.ch/site/assets/uploads/2018/02/ar4-wg1-chapter2-1.pdf.

IPCC, 2013. Climate Change 2013: Phys. Sci. Basis. https://www.ipcc.ch/report/ar5/wg1/.

IPCC, 2014. In: Stocker, T.F., Qin, D., Plattner, G.K., Tignor, M., Allen, S.K., Boschung, J., Nauels, A., Xia, Y., Bex, V., Midgley, P.M. (Eds.), Climate Change: the Physical Science Basis. Contribution of Working Group I to the Fifth Assessment Report of the Intergovernmental Panel on Climate Change. Cambridge University Press, Cambridge, United Kingdom and New York, NY, USA, 2013.

Johansson, J.K.E., Mellqvist, J., Samuelsson, J., Offerle, B., Moldanova, J., Rappenglück, B., Lefer, B., Flynn, J., 2014. Quantitative measurements and

modeling of industrial formaldehyde emissions in the Greater Houston area during campaigns in 2009 and 2011. JGR Atmospheres 119, 4303–4322. https://doi.org/10.1002/2013JD020159.

Karim, I., Rappenglück, B., 2023. Impact of Covid-19 lockdown regulations on PM2.5 and trace gases (NO_2, SO_2, CH_4, HCHO, $C_2H_2O_2$ and O_3) over Lahore, Pakistan. Atmos. Environ. 303, 119746. https://doi.org/10.1016/j.atmosenv.2023.119746.

Kavitha, M., Nair, P.R., Girach, I.A., Aneesh, S., Sijikumar, S., Renju, R., 2018. Diurnal and seasonal variations in surface methane at a tropical coastal station: role of mesoscale meteorology. Sci. Total Environ. 631–632, 1472–1485. https://doi.org/10.1016/j.scitotenv.2018.03.123, 2018.

Kerstel, E., 2004. Isotope ratio infrared spectrometry. In: de Groot, P.A. (Ed.), Handbook of Stable Isotope Techniques. Elsevier, Amsterdam, pp. 759–787.

Kerstel, E., Gianfrani, L., 2008. Advances in laser-based isotope ratio measurements: selected applications. Appl. Phys. B 92, 439–449. https://doi.org/10.1007/s00340-008-3128-x.

Kort, E.A., Frankenberg, C., Miller, C.E., Oda, T., 2012. Space-based observations of megacity carbon dioxide: space-based observations of megacity CO $_2$. Geophys. Res. Lett. 39. https://doi.org/10.1029/2012GL052738 n/a-n/a.

Kuwayama, T., Charrier-Klobas, J.G., Chen, Y., Vizenor, N.M., Blake, D.R., Pongetti, T., Conley, S.A., Sander, S.P., Croes, B., Herner, J.D., 2019. Source apportionment of ambient methane enhancements in Los Angeles, California, to evaluate emission inventory estimates. Environ. Sci. Technol. 53, 2961–2970. https://doi.org/10.1021/acs.est.8b02307.

Lal, R., 2013. Carbon sequestration, terrestrial. In: Reference Module in Earth Systems and Environmental Sciences. Elsevier. https://doi.org/10.1016/B978-0-12-409548-9.01211-2. B9780124095489012000.

Le Quéré, C., Andrew, R.M., Friedlingstein, P., Sitch, S., Hauck, J., Pongratz, J., Pickers, P.A., Korsbakken, J.I., Peters, G.P., Canadell, J.G., Arneth, A., Arora, V.K., Barbero, L., Bastos, A., Bopp, L., Chevallier, F., Chini, L.P., Ciais, P., Doney, S.C., Gkritzalis, T., Goll, D.S., Harris, I., Haverd, V., Hoffman, F.M., Hoppema, M., Houghton, R.A., Hurtt, G., Ilyina, T., Jain, A.K., Johannessen, T., Jones, C.D., Kato, E., Keeling, R.F., Goldewijk, K.K., Landschützer, P., Lefèvre, N., Lienert, S., Liu, Z., Lombardozzi, D., Metzl, N., Munro, D.R., Nabel, J.E.M.S., Nakaoka, S., Neill, C., Olsen, A., Ono, T., Patra, P., Peregon, A., Peters, W., Peylin, P., Pfeil, B., Pierrot, D., Poulter, B., Rehder, G., Resplandy, L., Robertson, E., Rocher, M., Rödenbeck, C., Schuster, U., Schwinger, J., Séférian, R., Skjelvan, I., Steinhoff, T., Sutton, A., Tans, P.P., Tian, H., Tilbrook, B., Tubiello, F.N., Van Der Laan-Luijkx, I.T., Van Der Werf, G.R., Viovy, N., Walker, A.P., Wiltshire, A.J., Wright, R., Zaehle, S., Zheng, B., 2018. Global carbon budget 2018. Earth Syst. Sci. Data 10, 2141–2194. https://doi.org/10.5194/essd-10-2141-2018.

Leuchner, M., Rappenglück, B., 2010. VOC source–receptor relationships in Houston during TexAQS-II. Atmos. Environ. 44, 4056–4067. https://doi.org/10.1016/j.atmosenv.2009.02.029.

Liu, M., van der A, R., van Weele, M., Eskes, H., Lu, X., Veefkind, P., de Laat, J., Kong, H., Wang, J., Sun, J., Ding, J., Zhao, Y., Weng, H., 2021. A New divergence method to quantify methane emissions using observations of sentinel-5P TROPOMI. Geophys. Res. Lett. 48. https://doi.org/10.1029/2021GL094151 e2021GL094151.

Li, X., Rappenglueck, B., 2018. A study of model nighttime ozone bias in air quality modeling. Atmos. Environ. 195, 210–228. https://doi.org/10.1016/j.atmosenv.2018.09.046.

Mavrovic, A., Sonnentag, O., Lemmetyinen, J., Baltzer, J.L., Kinnard, C., Roy, A., 2023. Reviews and syntheses: recent advances in microwave remote sensing in support of terrestrial carbon cycle science in Arctic–boreal regions. Biogeosciences 20, 2941–2970. https://doi.org/10.5194/bg-20-2941-2023.

Mastrogiacomo, J., Crippa, M., MacDonald, C.G., Roehl, C.M., Wunch, D., 2025. Estimating urban CH4 emissions from satellite-derived enhancement ratios of CH_4, CO_2, and CO. JGR Atmospheres 130. https://doi.org/10.1029/2025JD043394 e2025JD043394.

McKain, K., Wofsy, S.C., Nehrkorn, T., Eluszkiewicz, J., Ehleringer, J.R., Stephens, B.B., 2012. Assessment of ground-based atmospheric observations for verification of greenhouse gas emissions from an urban region. Proc. Natl. Acad. Sci. USA. 109, 8423–8428. https://doi.org/10.1073/pnas.1116645109.

Messerschmid, T.F.E., Wehling, J., Bobon, N., Kahmen, A., Klak, C., Los, J.A., Nelson, D. B., dos Santos, P., de Vos, J.M., Kadereit, G., 2021. Carbon isotope composition of plant photosynthetic tissues reflects a Crassulacean Acid Metabolism (CAM) continuum in the majority of CAM lineages. Perspectives in Plant Ecology. Evolution and Systematics 51, 125619. https://doi.org/10.1016/j.ppees.2021.125619.

MIT Climate, 2025. Experts say composting is the best solution to landfills. Where does Houston stand? MIT Climate. https://climate.mit.edu/posts/experts-say-composting-best-solution-landfills-where-does-houston-stand. (Accessed 12 May 2025).

Newman, S., Jeong, S., Fischer, M.L., Xu, X., Haman, C.L., Lefer, B., Alvarez, S., Rappenglueck, B., Kort, E.A., Andrews, A.E., Peischl, J., Gurney, K.R., Miller, C.E., Yung, Y.L., 2013. Diurnal tracking of anthropogenic CO_2 emissions in the Los Angeles basin megacity during spring 2010. Atmos. Chem. Phys. 13, 4359–4372. https://doi.org/10.5194/acp-13-4359-2013.

Pataki, D.E., Bowling, D.R., Ehleringer, J.R., 2003. Seasonal cycle of carbon dioxide and its isotopic composition in an urban atmosphere: anthropogenic and biogenic effects. J. Geophys. Res. 108, 4735. https://doi.org/10.1029/2003JD003865.

Pegov, S., 2008. Anthropospheric and anthropogenic impact on the biosphere. In: Encyclopedia of Ecology. Elsevier, pp. 1–7. https://doi.org/10.1016/B978-0-444-63768-0.09800-0.

Population Division, 2025. https://www.census.gov/data/tables/time-series/demo/popest/2020s-total-metro-and-micro-statistical-areas.html.

Ramachandran Nair, P.K., 2013. Agroforestry: trees in support of sustainable agriculture. In: Reference Module in Earth Systems and Environmental Sciences. Elsevier, pp. 123–135. https://doi.org/10.1016/B978-0-12-409548-9.05088-0.

Ramacher, M.O.P., Matthias, V., Aulinger, A., Quante, M., Bieser, J., Karl, M., 2020. Contributions of traffic and shipping emissions to city-scale NOx and PM2.5 exposure in Hamburg. Atmos. Environ. 237, 117674. https://doi.org/10.1016/j.atmosenv.2020.117674.

Rappenglück, B., Dasgupta, P.K., Leuchner, M., Li, Q., Luke, W., 2010. Formaldehyde and its relation to CO, PAN, and SO_2 in the Houston-Galveston airshed. Atmos. Chem. Phys. 10, 2413–2424.

Rappenglück, B., Lubertino, G., Alvarez, S., Golovko, J., Czader, B., Ackermann, L., 2013. Radical precursors and related species from traffic as observed and modeled at an urban highway junction. J. Air Waste Manag. Assoc. 63 (11), 1270–1286. https://doi.org/10.1080/10962247.2013.822438.

Rice, A., Bostrom, G., 2011. Measurements of carbon dioxide in an Oregon metropolitan region. Atmos. Environ. 45, 1138–1144. https://doi.org/10.1016/j.atmosenv.2010.11.026.

Rigby, M., Toumi, R., Fisher, R., Lowry, D., Nisbet, E.G., 2008. First continuous measurements of CO_2 mixing ratio in central London using a compact diffusion probe. Atmos. Environ. 42, 8943–8953. https://doi.org/10.1016/j.atmosenv.2008.06.040.

Sadeghi, B., Pouyaei, A., Choi, Y., Rappenglueck, B., 2022. Influence of seasonal variability on source characteristics of VOCs at Houston industrial area. Atmos. Environ. 277. https://doi.org/10.1016/j.atmosenv.2022.119077.

Sanchez, N.P., Zheng, C., Ye, W., Czader, B., Cohan, D.S., Tittel, F.K., Griffin, R.J., 2018. Exploratory study of atmospheric methane enhancements derived from natural gas use in the Houston urban area. Atmos. Environ. 176, 261–273. https://doi.org/10.1016/j.atmosenv.2018.01.001.

Skorokhod, A.I., Pankratova, N.V., Belikov, I.B., Thompson, R.L., Novigatsky, A.N., Golitsyn, G.S., 2016. Observations of atmospheric methane and its stable isotope ratio (δ13C) over the Russian Arctic seas from ship cruises in the summer and autumn of 2015. Dokl. Earth Sci. 470, 1081–1085. https://doi.org/10.1134/S1028334X16100160.

Statkewicz, M.D., Talbot, R., Rappenglueck, B., 2021. Changes in precipitation patterns in Houston, Texas. Environ. Adv. 5, 100073. https://doi.org/10.1016/j.envadv.2021.100073.

U.S. Bureau of Economic Analysis, 2024. https://fred.stlouisfed.org/release?et=&pageID=2&rid=397&t=. (Accessed 10 June 2025).

United Nations, Human Settlement Programme 2011: Hot Cities: Battle Ground for Climate Change, Washington, DC, USA.

United States Census Bureau, 2025. Metropolitan and micropolitan statistical areas population totals: 2020-2024". Population Division. March 13, 2025. Retrieved. (Accessed 20 June 2025).

Wang, T., 2020. Statista 2. https://www.statista.com/statistics/219343/cement-productionworldwide/#::text=Cement%20production%20reached%20an%20estimated,in%202019%20in%20the%20U.S.

Westmoreland, E.J., Carslaw, N., Carslaw, D.C., Gillah, A., Bates, E., 2007. Analysis of air quality within a street canyon using statistical and dispersion modelling techniques. Atmos. Environ. 41, 9195–9205. https://doi.org/10.1016/j.atmosenv.2007.07.057.

Wilmot, C.-S.M., Rappenglück, B., Li, X., Cuchiara, G., 2014. MM5 v3.6.1 and WRF v3.5.1 model comparison of standard and surface energy variables in the development of the planetary boundary layer. Geosci. Model Dev. (GMD) 7, 2693–2707. https://doi.org/10.5194/gmd-7-2693-2014.

WMO (World Meteorological Organization), 2023. The state of greenhouse gases in the atmosphere based on global observations through 2022. WMO Greenhouse Gas Bulletin (19).

Worrell, E., Price, L., Martin, N., Hendriks, C., Meida, L.O., 2001. Carbon dioxide emissions from the global cement industry Annu. Rev. Energy. Environ. Times 26, 303–329. https://doi.org/10.1146/annurev.energy.26.1.303.

Yang, S., Lan, X., Talbot, R., Liu, L., 2019. Characterizing anthropogenic methane sources in the Houston and Barnett Shale areas of Texas using the isotopic signature $\delta^{13}C$ in CH_4. Sci. Total Environ. 696, 133856. https://doi.org/10.1016/j.scitotenv.2019.133856.

Yu, K.N., Cheung, Y.P., Cheung, T., Henry, R.C., 2004. Identifying the impact of large urban airports on local air quality by nonparametric regression. Atmos. Environ. 38, 4501–4507. https://doi.org/10.1016/j.atmosenv.2004.05.034.